

# Self-consistent model of magnetospheric electric field, ring current, plasmasphere, and electromagnetic ion cyclotron waves: Initial results

K. V. Gamayunov,<sup>1</sup> G. V. Khazanov,<sup>2</sup> M. W. Liemohn,<sup>3</sup> M.-C. Fok,<sup>2</sup> and A. J. Ridley<sup>3</sup>

Received 10 July 2008; revised 23 December 2008; accepted 7 January 2009; published 28 March 2009.

[1] Further development of our self-consistent model of interacting ring current (RC) ions and electromagnetic ion cyclotron (EMIC) waves is presented. This model incorporates large-scale magnetosphere-ionosphere coupling and treats self-consistently not only EMIC waves and RC ions, but also the magnetospheric electric field, RC, and plasmasphere. Initial simulations indicate that the region beyond geostationary orbit should be included in the simulation of the magnetosphere-ionosphere coupling. Additionally, a self-consistent description, based on first principles, of the ionospheric conductance is required. These initial simulations further show that in order to model the EMIC wave distribution and wave spectral properties accurately, the plasmasphere should also be simulated self-consistently, since its fine structure requires as much care as that of the RC. Finally, an effect of the finite time needed to reestablish a new potential pattern throughout the ionosphere and to communicate between the ionosphere and the equatorial magnetosphere cannot be ignored.

**Citation:** Gamayunov, K. V., G. V. Khazanov, M. W. Liemohn, M.-C. Fok, and A. J. Ridley (2009), Self-consistent model of magnetospheric electric field, ring current, plasmasphere, and electromagnetic ion cyclotron waves: Initial results, *J. Geophys. Res.*, 114, A03221, doi:10.1029/2008JA013597.

## 1. Introduction

[2] Electromagnetic ion cyclotron (EMIC) waves are a common and important feature of the Earth's magnetosphere. The source of free energy for wave excitation is provided by the temperature anisotropy of ring current (RC) ions, which naturally develops during inward convection from the plasmasheet. The EMIC waves have frequencies below the proton gyrofrequency, and they are excited mainly in the vicinity of the magnetic equator with a quasi field-aligned wave normal angle [Cornwall, 1965; Kennel and Petschek, 1966]. These waves were observed in the inner [LaBelle *et al.*, 1988; Erlandson and Ukhorskiy, 2001] and outer [Anderson *et al.*, 1992a, 1992b] magnetosphere, at geostationary orbit [Young *et al.*, 1981; Mauk, 1982], at high latitudes [Erlandson *et al.*, 1990], and at ionospheric altitudes [Iyemori and Hayashi, 1989; Bräyvy *et al.*, 1998].

[3] Feedback from EMIC waves causes nonadiabatic pitch angle scattering of the RC ions (mainly protons) and their loss to the atmosphere, which leads to the decay of RC [Cornwall *et al.*, 1970]. This is especially important during the main phase of storms, when RC decay is possible with a time scale of around an hour or less [Gonzalez *et al.*, 1989]. During the main phase of major storms RC  $O^+$  may

dominate [Hamilton *et al.*, 1988; Daglis, 1997]. These ions cause damping of the  $He^+$ -mode EMIC waves, which may be very important for RC evolution during the main phase of the greatest storms [Thorne and Horne, 1994, 1997]. Obliquely propagating EMIC waves interact well with thermal plasmaspheric electrons due to Landau resonance [Thorne and Horne, 1992; Khazanov *et al.*, 2007b]. Subsequent transport of the dissipating wave energy into the ionosphere causes an ionospheric temperature enhancement [Gurgiolo *et al.*, 2005]. This wave dissipation is a mechanism proposed to explain stable auroral red arc emissions present during the recovery phase of storms [Cornwall *et al.*, 1971; Kozyra *et al.*, 1997]. Measurements taken aboard the Prognoz satellites revealed a so-called "hot zone" near the plasmopause, where a temperature of plasmaspheric ions can reach tens of thousands of degrees [Bezrukikh and Gringauz, 1976; Gringauz, 1983, 1985]. Nonlinear induced scattering of EMIC waves by thermal protons [Galeev, 1975] was used in the RC-plasmasphere interaction model by Gorbachev *et al.* [1992] in order to account for these observations. An extended analysis of thermal/suprathermal ion heating by EMIC waves in the outer magnetosphere was presented by Anderson and Fuselier [1994], Fuselier and Anderson [1996] and Horne and Thorne [1997]. Relativistic electrons ( $\geq 1$  MeV) in the outer radiation belt can also strongly interact with EMIC waves [Thorne and Kennel, 1971; Lyons and Thorne, 1972]. Data from balloon-borne X-ray instruments provides indirect but strong evidence that EMIC waves cause precipitation of outer-zone relativistic electrons [Foat *et al.*, 1998; Lorentzen *et al.*, 2000]. These observations stimulated theoretical and statistical studies,

<sup>1</sup>USRA, NASA Marshall Space Flight Center, Huntsville, Alabama, USA.

<sup>2</sup>NASA Goddard Space Flight Center, Greenbelt, Maryland, USA.

<sup>3</sup>Atmospheric, Oceanic, and Space Sciences Department, University of Michigan, Ann Arbor, Michigan, USA.

which demonstrated that EMIC wave-induced pitch angle diffusion of MeV electrons can operate in the strong diffusion limit with a time scale of several hours to a day [Summers and Thorne, 2003; Albert, 2003; Meredith et al., 2003]. This scattering mechanism is now considered to be one of the most important means for relativistic electron loss during the initial and main phases of storm. All of the above clearly demonstrates that EMIC waves strongly interact with electrons and ions of energies ranging from  $\sim 1$  eV to  $\sim 10$  MeV, and that these waves strongly affect the dynamics of resonant RC ions, thermal electrons and ions, and the outer radiation belt relativistic electrons. The effect of these interactions is nonadiabatic particle heating and/or pitch angle scattering, and loss to the atmosphere.

[4] The rate of ion and electron scattering/heating in the Earth's magnetosphere is not only controlled by the wave intensity-spatial-temporal distribution but also strongly depends on the spectral distribution of the wave power. Unfortunately, there are still very few satellite-based studies of EMIC waves, especially during the main phase of magnetic storms, and currently available observational information regarding EMIC wave power spectral density (mainly from the AMPTE/CCE and CRRES satellites) is poor [Engebretson et al., 2008]. Ideally, a combination of theoretical models and available-reliable data should be utilized to obtain the power spectral density of EMIC waves on a global magnetospheric scale throughout the different storm phases. To the best of our knowledge, there is only one model that is able to self-consistently simulate a spatial, temporal and spectral distribution of EMIC waves on a global magnetospheric scale during the different storm phases [Gamayunov and Khazanov, 2008]. This model is based on first principles, and explicitly includes the wave generation/damping, propagation, refraction, reflection and tunneling in a multi-ion magnetospheric plasma. The  $He^+$ -mode EMIC wave simulations based on this model have showed that the equatorial wave normal angles can be distributed in the source region, i.e., in the region of small wave normal angles, and also in the entire wave region, including those near  $90^\circ$ . The occurrences of the oblique and field-aligned wave normal angle distributions appear to be nearly equal with a slight dominance of oblique events [Khazanov and Gamayunov, 2007]. This theoretical prediction is supported by a large data set of the observed wave ellipticity [Anderson et al., 1992b; Fraser and Nguyen, 2001; Meredith et al., 2003]. The observation of a significant number of linearly polarized events near the equator suggests that waves are often highly oblique there. Using the more reliable wave step polarization technique, Anderson et al. [1996] and Denton et al. [1996] analyzed data from the AMPTE/CCE spacecraft, presented the first analysis of near linearly polarized waves for which the polarization properties were determined. They found a significant number of wave intervals with a wave normal angle  $\theta > 70^\circ$ , the highest  $\theta$  ever reported. Compared to field-aligned waves, such highly oblique wave normal angle distributions can dramatically change the effectiveness (by an order of magnitude or more) of both the wave-induced RC proton precipitation [Khazanov et al., 2007b] and relativistic electron scattering [Glauert and Horne, 2005; Khazanov and Gamayunov, 2007]. Strong sensitivity of the scattering rates to the wave spectral characteristics, and the wide distribution of EMIC

wave normal angles observed in the magnetosphere, suggests that in order to employ EMIC waves for heating and/or scattering of the magnetospheric particles in a model, the wave spectral distribution will require special care, and should be properly established.

[5] The resulting EMIC wave power spectral density depends on the RC and cold plasma characteristics. On the other hand, the convective patterns of both RC ions and the cold plasmaspheric plasma are controlled by the magnetospheric electric field, determining the conditions for the interaction of RC and EMIC waves. Therefore, this electric field is one of the most crucial elements necessary to properly determine the wave power spectral density. The region 2 field-aligned currents (FACs) couple the magnetosphere and ionosphere. This large scale coupling determines and maintains a self-consistent dynamic of the electric field and RC [Vasyliunas, 1970; Jaggi and Wolf, 1973; Garner et al., 2004; Fok et al., 2001; Khazanov et al., 2003b; Liemohn et al., 2004]. A self-consistent simulation of the magnetosphere-ionosphere system should provide, at least in principle, the most accurate theoretical electric field. The EMIC waves resulting in the magnetosphere are not only a passive element in the coupled RC-ionosphere system but also may influence the electrodynamics of coupling. During storm times, the wave-induced RC proton precipitation not only changes the FAC distribution, but can potentially modify the conductance and/or the neutral gas velocity in the ionosphere-thermosphere system [Galand et al., 2001; Galand and Richmond, 2001; Fang et al., 2007a, 2007b]. Both of these characteristics are crucial elements in the magnetosphere-ionosphere electrodynamics. Such wave-induced modification can be especially important equatorward of the low-latitude edges of the electron and proton auroral ovals where the wave-induced RC ion precipitation may be a dominant energy source. In addition, electrons and protons do not interact in the same way with the atmosphere. One should keep in mind that energetic protons ionize more efficiently than electrons do because their energy loss for each produced electron is smaller than that of energetic electrons [Galand et al., 1999]. Therefore, even if the proton energy flux is smaller compared to the electron flux, the response of the atmosphere to protons can be significant. The above arguments suggest that a self-consistent model of the magnetospheric electric field, RC, plasmasphere, and EMIC waves is needed to properly model wave spectral distribution and to improve the modeling of the large scale magnetosphere-ionosphere electrodynamics.

[6] In this study, we present a new computational model that is a result of coupling two RC models developed by our group. The first model deals with the large scale magnetosphere-ionosphere electrodynamic coupling and provides a self-consistent description of RC ions and the magnetospheric electric field [Liemohn et al., 2001; Ridley and Liemohn, 2002; Liemohn et al., 2004]. The second model is governed by a coupled system of the RC kinetic equation and the wave kinetic equation. This model self-consistently treats a mesoscale electrodynamic coupling of RC and EMIC waves, and determines the evolution of the EMIC wave power spectral density [Gamayunov and Khazanov, 2008]. The RC-EMIC wave model explicitly includes the wave growth/damping, propagation, refraction, reflection, and tunneling in a multi-ion magnetospheric plasma.

Although RC ions and EMIC waves in the second model are treated self-consistently, the electric field is externally specified. So far, the above two models were used independently. As such, the main purpose of this paper is to present a new self-consistent model of the magnetospheric electric field, RC, plasmasphere, and EMIC waves along with initial results from the model simulations. The results presented in this study were obtained from simulations of the 2–4 May 1998 geomagnetic storm, that we previously analyzed using an analytical formulation of the Volland-Stern electric field [Khazanov *et al.*, 2006, 2007b; Gamayunov and Khazanov, 2008].

[7] This article is organized as follows: In section 2 we present a complete set of the governing equations, and formulate the approaches used in the model simulations. In the same section, we specify the initial/boundary conditions, and the interplanetary/geomagnetic characteristics, which drive our model. In section 3 the initial results from these simulations and discussion are provided. Finally, in section 4 we summarize.

## 2. RC-EMIC Wave Model and Magnetosphere-Ionosphere Coupling

### 2.1. Governing Equations

[8] To simulate the RC dynamics we solve the bounce-averaged kinetic equation for the phase space distribution function of the major RC species ( $H^+$ ,  $O^+$ , and  $He^+$ ), as originally suggested in the models of Fok *et al.* [1993] and Jordanova *et al.* [1996]. The distribution function,  $F(r_0, \varphi, E, \mu_0, t)$ , depends on the radial distance in the magnetic equatorial plane  $r_0$ , geomagnetic east longitude, kinetic energy  $E$ , cosine of the equatorial pitch angle  $\mu_0$ , and time  $t$ . For the  $He^+$ -mode EMIC waves we also use the bounce-averaged kinetic equation. This equation describes a physical model of EMIC waves bouncing between the off-equatorial magnetic latitudes, which correspond to the bi-ion hybrid frequencies in conjugate hemispheres, along with tunneling across the reflection zones and subsequent strong absorption in the ionosphere (for the observational and theoretical justifications of this model see [Gamayunov and Khazanov, 2008; Khazanov *et al.*, 2007a]). The bounce-averaged wave kinetic equation was derived in our previous paper [Khazanov *et al.*, 2006], and it explicitly includes the EMIC wave growth/damping, propagation, refraction, reflection, and wave tunneling in a multi-ion magnetospheric plasma. In the present study, following Khazanov *et al.* [2006], we ignore the azimuthal and radial drifts of the wave packets during propagation, we do not include the wave tunneling across the stop zone, and consequently use a truncated wave kinetic equation. The resulting system of equations to drive RC-EMIC wave coupling takes the form:

$$\begin{aligned} \frac{\partial F}{\partial t} + \frac{1}{r_0^2} \frac{\partial}{\partial r_0} \left( r_0^2 \left\langle \frac{dr_0}{dt} \right\rangle F \right) + \frac{\partial}{\partial \varphi} \left( \left\langle \frac{d\varphi}{dt} \right\rangle F \right) \\ + \frac{1}{\sqrt{E}} \frac{\partial}{\partial E} \left( \sqrt{E} \left\langle \frac{dE}{dt} \right\rangle F \right) + \frac{1}{\mu_0 h(\mu_0)} \\ \cdot \frac{\partial}{\partial \mu_0} \left( \mu_0 h(\mu_0) \left\langle \frac{d\mu_0}{dt} \right\rangle F \right) = \left\langle \left( \frac{\delta F}{\delta t} \right)_{loss} \right\rangle, \end{aligned} \quad (1)$$

$$\frac{\partial B_w^2(r_0, \varphi, t, \omega, \theta_0)}{\partial t} + \langle \dot{\theta}_0 \rangle \frac{\partial B_w^2}{\partial \theta_0} = 2 \langle \gamma(r_0, \varphi, t, \omega, \theta_0) \rangle B_w^2. \quad (2)$$

On the left-hand side of equation (1), all the bounce-averaged drift velocities are denoted as  $\langle \dots \rangle$  and may be found in many previous studies [e.g., Khazanov *et al.*, 2003a]. The term on the right-hand side of this equation includes losses from charge exchange, Coulomb collisions, RC-EMIC wave scattering, and ion precipitation at low altitudes [e.g., Khazanov *et al.*, 2003a]. Loss through the dayside magnetopause is taken into account, allowing a free outflow of the RC ions from the simulation domain. In equation (2),  $B_w$  is the EMIC wave spectral magnetic field,  $\omega$  and  $\theta_0$  are the wave frequency and equatorial wave normal angle, respectively,  $\langle \dot{\theta}_0 \rangle$  is the bounce-averaged drift velocity of the wave normal angle, and  $\langle \gamma \rangle$  is a result of averaging the local growth/damping rate along the ray phase trajectory over the entire wave bounce period. The factor  $\langle \gamma \rangle$  takes into account both the wave energy source due to interaction with the RC ions and the energy sink due to absorption by thermal and hot plasmas.

[9] To perform bounce averaging in equation (2), the ray phase trajectory should be known, and we obtain it by solving the set of ray tracing equations. For a plane geometry these equations can be written as [e.g., Haselgrove, 1954; Haselgrove and Haselgrove, 1960; Kimura, 1966; Gamayunov and Khazanov, 2008]

$$\frac{dr}{dt} = - \frac{(\partial G / \partial \mathbf{k})_r}{\partial G / \partial \omega}, \quad (3)$$

$$r \frac{d\lambda}{dt} = - \frac{(\partial G / \partial \mathbf{k})_\lambda}{\partial G / \partial \omega}, \quad (4)$$

$$\frac{dk_r}{dt} = k_\lambda \frac{d\lambda}{dt} + \frac{(\partial G / \partial \mathbf{r})_r}{\partial G / \partial \omega}, \quad (5)$$

$$\frac{dk_\lambda}{dt} = - \frac{k_\lambda}{r} \frac{dr}{dt} + \frac{(\partial G / \partial \mathbf{r})_\lambda}{\partial G / \partial \omega}. \quad (6)$$

In equations (3)–(6), the Earth-centered polar coordinate system is used to characterize any point  $P$  on the ray trajectory by length of the radius vector,  $r$ , and magnetic latitude,  $\lambda$ . Two components,  $k_r$  and  $k_\lambda$ , of the wave vector are given in a local Cartesian coordinate system centered on the current point  $P$  with its axes oriented along the radius vector and magnetic latitude direction, respectively. The function  $G(\omega, \mathbf{k}, \mathbf{r})$  has roots for EMIC eigenmodes only, i.e.,  $G = 0$  at any point along the EMIC wave phase trajectories. Equations (3)–(6) are also used to obtain the off-equatorial power spectral density distribution for EMIC waves, which is needed to calculate the bounce-averaged pitch angle diffusion coefficient in the right-hand side of equation (1). (For more details about the system of equations (1)–(6) and its applicability, please see our previous papers [Khazanov *et al.*, 2003a, 2006, 2007a].)

[10] The bounce-averaged pitch angle diffusion coefficient on the right-hand side of equation (1) is a functional form of the EMIC wave power spectral density, and  $\langle \gamma(r_0, \varphi, t, \omega, \theta_0) \rangle$  in equation (2) is a functional form of the phase space distribution function. So, there is a system of coupled



equations, and the entire set of equations (1)–(6) self-consistently describes the interacting RC and EMIC waves in a quasilinear approximation. Compared to our previous RC-EMIC wave studies, which are based on equations (1)–(6) only [Khazanov *et al.*, 2006, 2007b], we are now going to take into account the magnetosphere-ionosphere coupling by self-consistently treating the current closure between RC and the ionosphere.

[11] *Vasyliunas* [1970] mathematically formulated a self-consistent model of the magnetosphere-ionosphere coupling by providing the basic equations governing the system. He outlined a logical chain of the model as follows: (1) the magnetospheric electric field determines the distribution of RC ions and electrons and, particularly, the total plasma pressure at any point; (2) from the plasma pressure gradients, the electric current perpendicular to the magnetic field can be calculated; (3) because the total current density should have zero divergence under magnetospheric conditions, the divergence of the perpendicular current density must be canceled by the divergence of FAC density, and so the divergence of the perpendicular current integrated along the entire field line gives the total FAC flowing into/out of the conjugate ionospheres; (4) from the requirement that FAC is closed by the horizontal ohmic currents in the ionosphere, the distribution of the electric potential in the ionosphere can be found; and (5) the ionospheric potential can be mapped back into the magnetosphere along geomagnetic field lines, and the requirement that this “new” magnetospheric electric field agrees with the “initial” magnetospheric field closes the magnetosphere-ionosphere system.

[12] To quantify the above logical chain, *Vasyliunas* [1970] used the following equations:

$$\mathbf{J}_\perp(r_0, \varphi, s) = \frac{\mathbf{B}}{B^2} \times \left( \nabla P_\perp + \frac{P_\parallel - P_\perp}{B^2} (\mathbf{B} \cdot \nabla) \mathbf{B} \right), \quad (7)$$

$$J_{\parallel,i}(\lambda(r_0), \varphi) = -B_i(\lambda(r_0), \varphi) \int_{s_S}^{s_N} \frac{\nabla \mathbf{J}_\perp}{B(r_0, \varphi, s)} ds, \quad (8)$$

$$\nabla \mathbf{I}_i = j_{\parallel,i} \sin \chi, \quad \mathbf{I}_i = \Sigma \left( -\nabla \Phi_i + \frac{\mathbf{V}_n}{c} \times \mathbf{B}_i \right), \quad (9)$$

where  $P_\perp$  and  $P_\parallel$  are the total plasma pressure (we neglect the electron pressure in the current study) perpendicular and parallel to the external magnetic field  $\mathbf{B}$ , respectively, and  $\mathbf{J}_\perp$  is the perpendicular current density. The FAC density at the ionospheric level is  $J_{\parallel,i}$  (positive for current flowing into the ionosphere),  $B_i$  is the magnetic field in the ionosphere, and integration in equation (8) is done along the entire magnetic field line between foot points  $s_S$  and  $s_N$ . The coordinates  $(\lambda(r_0), \varphi)$  are the corresponding ionospheric latitude and MLT for the magnetic field line crossing the equatorial plane at  $(r_0, \varphi)$  (assuming that  $\varphi$  is the same at the equator and at the ionospheric altitude). In equations (9),  $\mathbf{I}_i$  and  $\Sigma$  are the height integrated horizontal ionospheric current density and conductivity tensor, respectively, and  $\chi$  is an inclination of the magnetic field (dip angle). The electric potential at the ionosphere level is  $\Phi_i$ , and  $\mathbf{V}_n$  is the

velocity of the neutral gas in the ionosphere. Following many previous studies, in the present study we assume that the neutral gas corotates with the Earth and neglect the potential drop between the ionosphere and the equatorial magnetosphere [e.g., *Ebihara et al.*, 2004]. Finally, it should be noted that, in general, equation (9) is written for the northern and southern ionospheres with the corresponding FAC  $j_{\parallel,i}$ , while equation (8) gives only the total FAC flowing into/out of the conjugate ionospheres but the obvious equation  $J_{\parallel,i} = j_{\parallel,i}(s_S) + j_{\parallel,i}(s_N)$  is held.

[13] The set of equations (1)–(9) drives the RC, the EMIC waves, and the magnetospheric electric field in a self-consistent manner if all the initial and boundary conditions are specified and the ionospheric Hall and Pedersen conductances are known. A block diagram of the self-consistent coupling of the RC, EMIC waves, plasmasphere, and ionosphere is presented in Figure 1. The system characteristics in orange boxes are externally specified, and the dashed lines connect the model elements, which are currently not linked.

## 2.2. Approaches Used in Simulations

[14] The geomagnetic field used in the present study is taken to be a dipole field. It is a reasonable approximation for the present study because the most important results are obtained from simulations of the 2–3 May 1998 period ( $Dst = -106$  nT) when the Earth’s magnetic field is only slightly disturbed in the inner magnetosphere [e.g., *Tsyganenko et al.*, 2003]. The convection electric field is calculated self-consistently as described in section 2.1, and the total electric field includes the magnetospheric convection and corotation field. The equatorial cold electron density,  $n_{e_c}$ , is obtained from the dynamic global core plasma model of *Ober et al.* [1997]. This model is basically the same as a time-dependent model of *Rasmussen et al.* [1993], which was used in our previous studies, except the Ober *et al.* model is linked with a self-consistent electric field obtained from the system (1)–(9), while the Rasmussen *et al.* model is driven by the Volland-Stern convection field [Volland, 1973; Stern, 1975] with  $Kp$  parameterization. Thus, the cold plasma density dynamics is also electrically self-consistent in our global RC-EMIC wave model. This is extremely important for a correct description of the EMIC wave generation/damping and propagation. In order to model the EMIC wave propagation and interaction with RC, we also need to know the density distribution in the meridional plane. In the present study we use a magnetic field model for the meridional density distribution, i.e.,  $n_e \sim B$ , because a more sophisticated analytical model by *Angerami and Thomas* [1964] used in our previous studies [e.g., *Khazanov et al.*, 2006] was found to give nearly the same results. The meridional model is then adjusted to the equatorial density model. So the resulting plasmaspheric model provides a 3D spatial distribution of the electron density. Besides electrons, the cold magnetospheric plasma is assumed to consist of 77%  $H^+$ , 20%  $He^+$ , and 3%  $O^+$ , which are in the range of 10–30% for  $He^+$  and 1–5% for  $O^+$  following the observations by *Young et al.* [1977] and *Horwitz et al.* [1981]. Geocoronal neutral hydrogen number densities, needed to calculate loss due to charge exchange, are obtained from the spherically symmetric model of *Chamberlain* [1963] with its parameters given by *Rairden et al.* [1986].

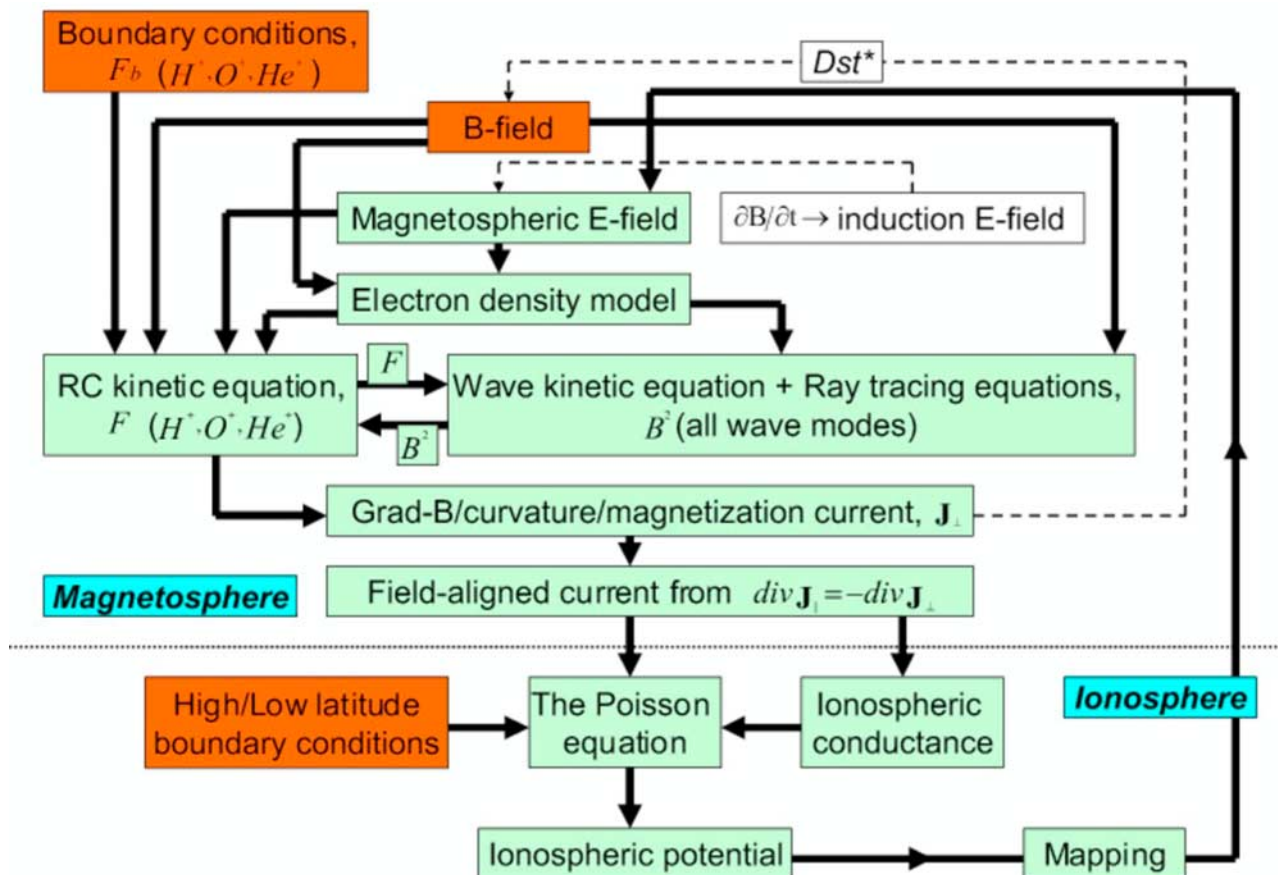


**Figure 1.** The block diagram of the RC, EMIC waves, plasmasphere, and ionosphere coupling in our model. The system characteristics in orange boxes are externally specified, and the dashed lines connect the model elements that are currently not linked.

[15] During the main phase of major storms, RC  $O^+$  may dominate [e.g., *Hamilton et al.*, 1988; *Daglis*, 1997] and, as a result, contribute to strong damping of the  $He^+$ -mode EMIC waves [*Thorne and Horne*, 1997]. Although there is no doubt that, in principle, this process is important, let us evaluate the validity of excluding the  $He^+$ -mode damping by RC  $O^+$  in the 2–4 May 1998 storm simulation. Using the RC kinetic model of *Jordanova et al.* [1998], *Farrugia et al.* [2003] found that during the main phase of the 4 May 1998 storm the energy density of RC  $H^+$  is greater than twice that of  $O^+$  at all MLTs, and the contribution of  $He^+$  to the RC energy content is negligible. This implies that the RC  $O^+$  content does not exceed 30% during the main phase of this storm. This estimate was obtained from a global simulation, which did not include oxygen band waves. On the other hand, *Bräysy et al.* [1998] observed a very asymmetric  $O^+$  RC during the main phase of the 2–8 April 1993 storm, which may suggest that a majority of the RC oxygen ions get lost before they reach the dusk MLT sector. This result is difficult to explain in terms of charge exchange and Coulomb scattering, and suggests that the production of EMIC waves contributes significantly to RC  $O^+$  decay during the main and early recovery phases. In other words, due to the generation of the  $O^+$ -mode EMIC waves, most RC  $O^+$  might precipitate before reaching the dusk MLT sector [*Bräysy et al.*, 1998]. Therefore, to estimate the RC  $O^+$

content correctly, the  $O^+$ -mode should be included in the simulation, and it is likely that *Farrugia et al.* [2003] overestimated the RC  $O^+$  content during 4 May 1998. Moreover, the calculations of *Thorne and Horne* [1997] clearly demonstrated that even the RC  $O^+$  percentage noted above cannot significantly suppress the resulting growth; inclusion of 26%  $O^+$  in the RC population causes the net wave gain to decrease by only 20%. In addition, the most important results shown in the present study are obtained from simulations of the 2–3 May 1998 period, i.e., the first main ( $Dst = -106$  nT) and recovery phases of the May 1998 large storm, when the RC  $O^+$  content should be even smaller than the *Farrugia et al.* estimate for 4 May 1998. It is for these reasons that we chose to exclude RC  $O^+$  in the present simulations, and to assume that the RC is entirely comprised of energetic protons.

[16] Equation (9) must be solved taking into account the contributions from both the northern and southern ionosphere. Because in the present study we assume the magnetic field lines to be equipotentials, the northern and southern ionospheres can just be replaced by an effective single ionosphere with  $\Sigma = \Sigma_S + \Sigma_N$ , and total FAC  $J_{\parallel,i}$  flowing into/out of it. After the resulting equation is solved, and  $\Phi_i$  is found, we can easily calculate the FACs  $j_{\parallel,i}(s_S)$

and  $j_{\parallel,i}(s_N)$  flowing into/out the southern and northern ionosphere.

[17] The ionospheric Hall and Pedersen conductances in our model are not calculated self-consistently but rather specified by empirical models. The resulting conductance arises from four sources: (1) direct solar extreme ultraviolet (EUV), (2) scattered solar EUV on both sides of the terminator, (3) starlight, and (4) auroral particle precipitation. The direct solar conductance is controlled by the solar zenith angle and the solar UV and EUV radiations, which correlate with the solar radio flux index  $F_{10.7}$ . In the present study we use the empirical model of *Moen and Brekke* [1993] for determining direct solar conductance. The scattered solar EUV and starlight conductance models are taken from the study of *Rasmussen and Schunk* [1987]. In order to specify the conductance from auroral precipitation, we use either the *Hardy et al.* [1987] statistical model or an empirical relationship between the FACs and the local Hall and Pedersen conductance established by *Ridley et al.* [2001, 2004]. The Hardy et al. model is compiled from the electron precipitation patterns obtained by the DMSP satellites and gives the Hall and Pedersen conductance as a function of MLT and magnetic latitude for seven levels of activity as measured by  $Kp$ . The Ridley et al. relationship was derived using the assimilative mapping of ionospheric electrodynamics (AMIE) technique [*Richmond and Kamide*, 1988]. The AMIE technique was run at a 1-min cadence for the entire month of January 1997, using 154 magnetometers. This resulted in almost 45000 2D maps of the Hall and Pedersen conductances and FAC. The conductance was derived from the *Ahn et al.* [1998] formulation, which relates ground-based magnetic perturbations to the Hall and Pedersen conductances. The Ridley et al. analysis showed an exponential relationship between the local FAC and the conductance [see *Amm*, 1996; *Goodman*, 1995]:

$$\Sigma = \Sigma_0 e^{-A|j_{\parallel,i}|}, \quad (10)$$

where the constants  $\Sigma_0$  and  $A$  are independent of the magnitude of  $j_{\parallel,i}$ , but depend on location and whether the current is upward or downward. Although the Ridley et al. relationship is entirely empirical and not based on first principles, by using it we introduce into the model at a degree of self-consistency between the ionospheric conductance and FAC. This is a principle modification because a self-consistent description of the ionospheric conductance makes equation (9) nonlinear compared to the case of statistical conductance model. For previous use of the Ridley et al. relationship in the RC simulation see *Liemohn et al.* [2005].

[18] To conclude this section, we note that the numerical implementations used to solve equations (1)–(6) are described in details in our previous publications [*Khazanov et al.*, 2003a, 2006], and to solve equation (9) a preconditioned gradient reduction resolution (GMRES) solver is used [*Ridley et al.*, 2004]. The GMRES method is robust enough to handle a wide variety of FAC and conductance patterns.

### 2.3. Initial and Boundary Conditions

[19] The initial RC distribution is constructed from the statistically derived quiet time RC proton energy distribu-

tion of *Sheldon and Hamilton* [1993] and the pitch angle characteristics of *Garcia and Spjeldvik* [1985]. The night-side boundary condition for equation (1) is imposed at the geostationary distance, and it is obtained using flux measurements from the Magnetospheric Plasma Analyzer [*Bame et al.*, 1993] and the Synchronous Orbit Particle Analyzer [*Belian et al.*, 1992] instruments on the geosynchronous LANL satellites during the modeled event. Then, according to *Young et al.* [1982] and *Liemohn et al.* [1999], we divide the total flux measured at geostationary orbit between the RC  $H^+$ ,  $O^+$ , and  $He^+$  depending on geomagnetic and solar activity as measured by  $Kp$  and  $F_{10.7}$  indices. Only the  $H^+$  flux is used as a boundary condition in the simulation.

[20] In the present study, the poleward boundary for equation (9) is taken at magnetic latitude  $\lambda = 69^\circ$ . On this boundary, we specify the electric potential using either the *Weimer* [1996] statistical model (hereinafter the W96 model), which is driven by the interplanetary magnetic field (IMF)  $B_y$ ,  $B_z$  components and solar wind velocity, or the convection model of *Volland and Stern* [1973; *Stern*, 1975] with  $Kp$  parameterization given by *Maynard and Chen* [1975] and shielding factor of 2 (hereinafter the VS model). The second boundary condition is specified at  $\lambda = 30^\circ$ , and we use either the W96 model or the VS model, both of which give the potential close to zero at that latitude. It should be noted that the result of calculation is insensitive to the choice of the lower boundary condition, as demonstrated by *Wolf* [1970]. So, the magnetospheric electric field is calculated self-consistently in the domain  $30^\circ < \lambda < 69^\circ$ . At the same time, we should emphasize that, compared to RC, the cold electron density is modeled in a more extended domain of  $L \leq 10$ , and in order to specify the electric field in the entire  $L \leq 10$  region, we use either the W96 or the VS model for the magnetic latitude above  $\lambda = 69^\circ$ .

[21] The initial RC, plasmasphere, and EMIC wave distributions are derived independently and, moreover, they have nothing to do with a particular state of the magnetosphere/plasmasphere system during a simulated event. Only the boundary conditions provided by the LANL satellites can be considered as data reflecting a particular geomagnetic situation (and, to a certain extent, the employed ionospheric conductance model and an imposed cross polar cap potential drop). Therefore, before the simulation of a particular geomagnetic event can occur, we first must find an appropriate initial state for the RC, electric field, plasmasphere, and EMIC waves that is self-consistent and reflects the particular geomagnetic situation. To obtain the self-consistent initial distributions for the entire system, we first prepared the plasmasphere by running the Ober model for 20 quiet days. Then, at 0000 UT on 1 May 1998, a simulation of equations (1)–(10) was started using all the controlling parameters and the initial/boundary conditions along with a background noise level for the  $He^+$ -mode EMIC waves [e.g., *Akhiezer et al.*, 1975]. We ran the model code for 24 hours to achieve a quasi self-consistent state for the system. Note that 24 hours has nothing to do with the typical time for wave amplification and instead reflects the minimum time needed to adjust the RC and waves to each other and to the real prehistory of a storm. The self-consistent modeling of the May 1998 storm period was started at 0000 UT on 2 May (24 hours after 1 May 0000 UT) using solutions of equations (1), (2), and the cold



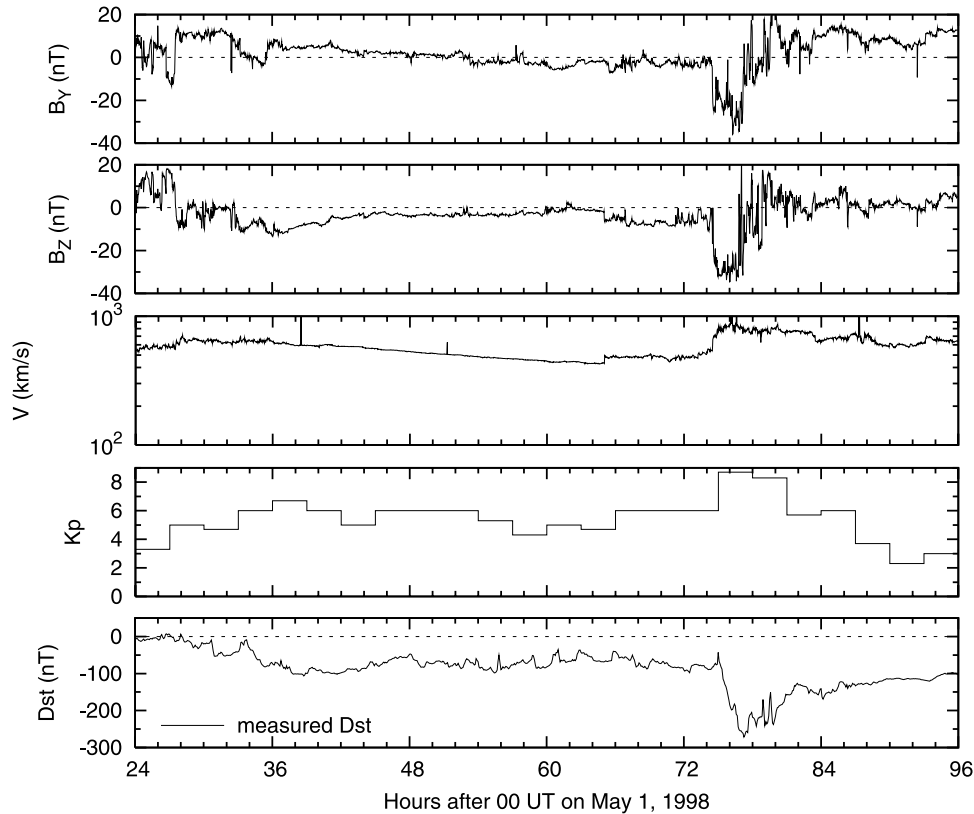


**Figure 2.** The interplanetary and geomagnetic characteristics during 2–4 May 1998. (top to bottom) The interplanetary magnetic field GSM  $B_Y$  and  $B_Z$  components, the solar wind velocity, 3-h  $K_p$  index, and the measured  $Dst$  index. The hours shown are counted from 0000 UT on 1 May 1998.

plasma distribution at 2400 UT on 1 May as the initial conditions for further simulation.

#### 2.4. Interplanetary and Geomagnetic Drivers for the Model

[22] The ionospheric boundary condition in our simulations is driven either by IMF  $B_Y$ ,  $B_Z$  components and solar wind velocity (the W96 model) or the 3-h  $K_p$  index (the VS model). The *Hardy et al.* [1987] ionospheric conductance model is driven by  $K_p$ . All of these driving parameters are shown in Figure 2 during the 2–4 May 1998 period. Interplanetary data are obtained from the Magnetic Field Investigation [Lepping *et al.*, 1995] and the Solar Wind Experiment [Ogilvie *et al.*, 1995] instruments aboard the WIND satellite. The interplanetary configuration of 1–5 May 1998 consists of a coronal mass ejection (CME) interacting with a trailing faster stream [Farrugia *et al.*, 2003]. The CME drives an interplanetary shock observed by the instruments aboard the WIND spacecraft at about 2220 UT on 1 May. Three episodes of the large negative IMF  $B_Z$  component were monitored. The first episode started at  $\sim$ 0330 UT on 2 May (27.5 hours after 1 May, 0000 UT), the second at 0230 UT on 4 May (74.5 hours after 1 May, 0000 UT), and the third (not shown) at  $\sim$ 0200 UT on 5 May (98 hours after 1 May, 0000 UT). These caused a “triple-dip” storm with the minimums  $Dst = -106$  nT,  $Dst = -272$  nT, and  $Dst = -153$  nT (not shown). The planetary  $K_p$  index reached maximum values

of  $K_p \approx 7^-$  and  $K_p \approx 9^-$  at the times when  $Dst$  minimums were recorded.

### 3. Results and Discussion

#### 3.1. Magnetospheric Electric Field

[23] The cross polar cap potential (CPCP) drop gives a rough quantitative assessment of the strength of convection in the inner magnetosphere. We calculate the CPCP drop as a difference between the maximum and minimum values of the potential at  $\lambda = 67.5^\circ$  (at  $L \approx 7$ ). Results of our calculations are shown in Figure 3. The lines in red, green, and blue show results from a self-consistent simulation, while the CPCP drop shown in black is for reference purposes only. Note that the red line lies somewhat higher than the black one. This is because we do not calculate FACs between  $\lambda = 69^\circ$  and  $\lambda = 67.5^\circ$  in the present simulations, and so there is no shielding taken into account unlike in the analytical formulation of the VS potential (black line in Figure 3). When the W96 model is imposed at  $\lambda = 69^\circ$ , the CPCP drops are very similar for both conductivity models, and the blue line is just slightly higher than the green one. The CPCP drop resulting from the VS model is larger during the majority of 2–4 May except for about 13 hours on 2 May and 12 hours on 4 May, when the CPCP drop from the W96 model is greater. It is seen that the W96 potential drop spikes to 300 kV during the main phase on 4 May, whereas the VS boundary condition results in a maximum CPCP drop of only 150 kV.

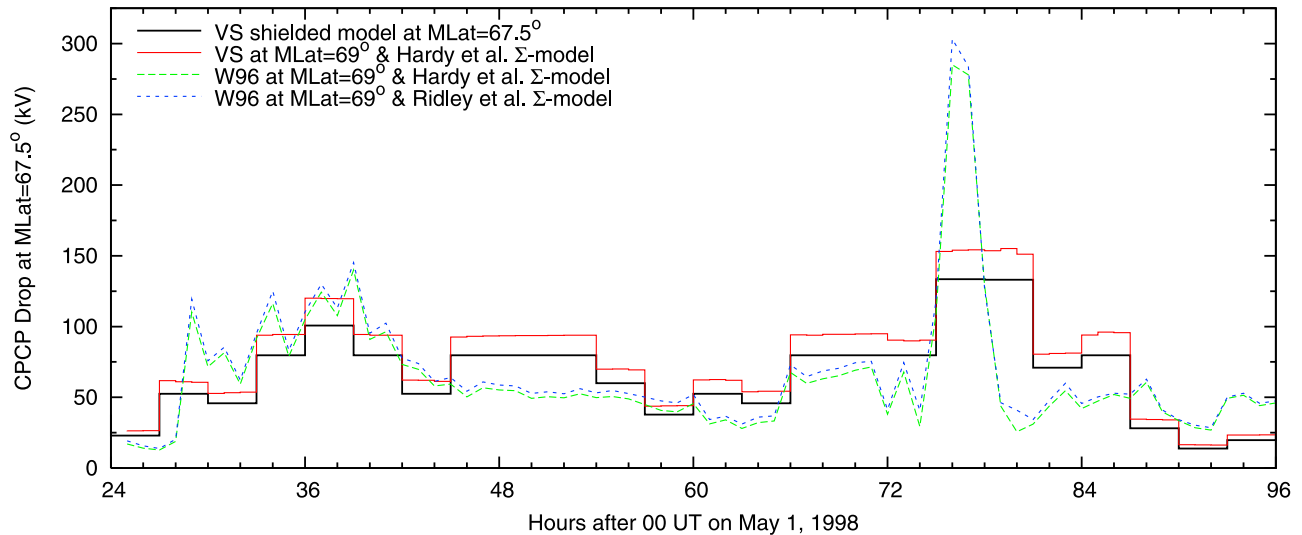


**Figure 3.** The cross polar cap potential drop from differently driven convection models during 2–4 May 1998. The black line, shown for reference, is the potential drop from the shielded Volland-Stern model with  $Kp$  parameterization. The red, green, and blue lines represent the self-consistent results obtained with either the VS or W96 model imposed at  $\lambda = 69^\circ$ , and either the Hardy et al. conductance model or the Ridley et al. empirical relationship between the FAC and conductance (see legend in Figure 3). In order to drive the W96 model, a 30-min time lag between WIND and the high latitude ionospheric boundary is adopted after *Farrugia et al.* [2003].

[24] Although the CPCP drop may serve as an overall measure of the convective strength, it does not give the morphology and strength of the electric field in the inner magnetosphere. To provide such insight, we selected six snapshots of the equatorial electric field patterns from 2 May, and one snapshot at hour 77 (0500 UT on 4 May). The corresponding electric potential contours are shown in Figure 4. The view is over the North Pole with local noon to the left. We present results for three runs. The equipotentials from a simulation with the VS model at the high latitude ionospheric boundary and the Hardy et al. conductance are shown in Figure 4 (top). The other two runs are performed with the W96 model applied at  $\lambda = 69^\circ$ , and differ only by the conductance model assumed. Figure 4 (middle) shows results for the Hardy et al. conductance model, while Figure 4 (bottom) is for a case when the Ridley et al. empirical relationship between the FAC and conductance is used. The potential configurations in Figure 4 are similar to those from the Rice Convection Model [e.g., *Garner et al.*, 2004]. Overall, there are qualitatively the same large-scale potential distributions in all three models, presented in Figure 4, with a well defined large-scale dawn-to-dusk electric field. Despite this, the potential patterns reveal large differences in both the magnitude of the potential and the shape of the contours. This suggests a difference in the fine structure of the electric field distribution since this field is proportional to the gradient of the potential.

[25] One obvious feature observed in Figure 4 is a significantly enhanced electric field in the region  $L \approx 3-4$  in the dusk–postmidnight MLT sector at hour 77 (and, not shown, at hour 76). This radially narrow intensification of the radial electric field (poleward electric field in the ionosphere) creates a westward flow channel, mainly in

the dusk-to-midnight MLT sector, while a region of westward (antisunward) convection is also observed in the postmidnight sector equatorward of  $L = 3$  (see Figure 4). This westward flow channel has come to be called the subauroral polarization stream (SAPS) [*Foster and Burke*, 2002; *Foster and Vo*, 2002]. The SAPS effect arises from the region 2 FACs, which flow down into the subauroral ionosphere and close the region 1 FACs through the poleward Pedersen currents. Because of the low conductance at subauroral latitudes, the Pedersen current generates an intense poleward electric field between the region 2 FAC and the low-latitude edge of the auroral particle precipitation [*Southwood and Wolf*, 1978; *Anderson et al.*, 1991, 1993; *Ridley and Liemohn*, 2002; *Mishin and Burke*, 2005].

[26] To show the potential structure and electric field inside the SAPS region, we took two meridional cuts across the entire simulation domain and the corresponding results are shown in Figure 5. Figures 5a and 5b show the potential profiles on the dawn-dusk meridian for hours 33 and 77. Results for three simulations are presented along with a profile for the analytical VS model. The corresponding equatorial radial electric fields are shown in Figures 5c and 5d for MLT = 18. Only a slight electric field intensification ( $<2.7$  mV/m) is observed in the dusk sector for hour 33 (see Figure 5c), while we see an extremely developed SAPS in Figure 5d ( $<13.4$  mV/m). The strongest electric field intensification in Figure 5d takes place for cases when the W96 model is used in combination with either the Hardy et al. conductance model or the Ridley et al. relationship. In the latter case, we see a slightly stronger electric field in the dusk MLT sector and a developed dawnside electric field of about 5 mV/m (see Figure 5b).

[27] Although the SAPS localization is correctly predicted by our model, it is likely that the SAPS electric field



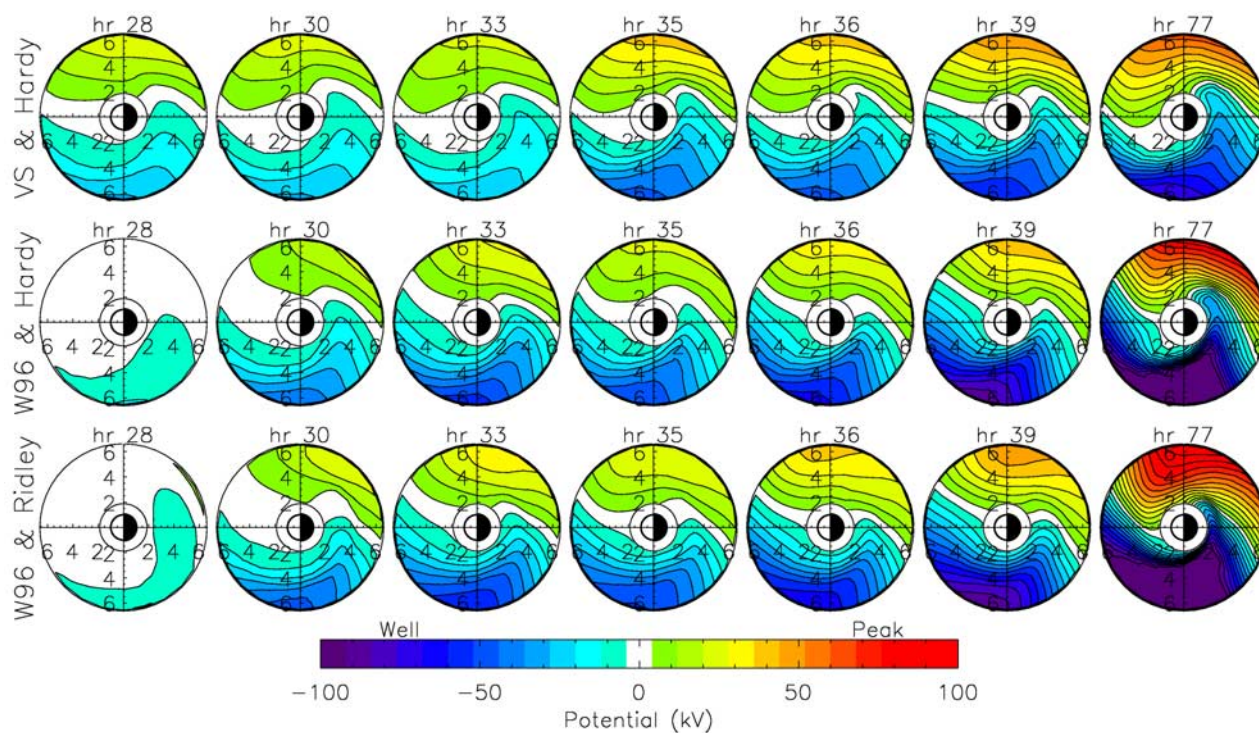


**Figure 4.** The equatorial potential contours in the inner magnetosphere without corotation field. The view is over the North Pole with local noon to the left. All of the indicated hours are counted from 0000 UT on 1 May 1998. (top) Results from a simulation with the VS model at the high latitude ionospheric boundary and the Hardy et al. conductance model. (middle) Simulation with the W96 model at  $\lambda = 69^\circ$  and the Hardy et al. conductance model. (bottom) The same as in Figure 4 (middle) except that the Ridley et al. empirical relationship between the FAC and the local Hall/Pedersen conductance is used. Equipotentials are drawn every 8 kV.

in Figure 5d is overestimated for the W96 boundary condition. Indeed, from the statistical model based on the electric field data measured by the Akebono/EFD instrument, *Nishimura et al.* [2007] derived the equatorial  $E_y$  electric field component in the dusk SAPS region to be 6 mV/m during the main phase of storm. It should be noted, however, that the SAPS electric field can sometimes reach more than 10 mV/m during the main phase of geomagnetic storms [*Shinbori et al.*, 2004], and the CPCP drop derived by *Nishimura et al.* [2007] is 180 kV, whereas in our simulation it is 300 kV. The measurements taken by the double-probe electric field instrument on board the CRRES spacecraft show a similar electric field magnitude [*Wygant et al.*, 1998]. There are at least two reasons that may lead to an overestimation of the SAPS electric field in our simulations. (1) Because the W96 model was constructed from data with IMF under 10 nT, this model essentially overestimates the CPCP drop during the 4 May event when IMF was around 40 nT [e.g., *Burke et al.*, 1998]. (2) In the present simulations, we did not take into account the FACs beyond geostationary orbit, which may contribute essentially to the shielding of midlatitudes from a high latitude driving convection field; the effect of FAC is proportional to the volume of the magnetic flux tube, and from the estimate by *Vasyliunas* [1972] the effect of FAC at  $L = 6.6$  is about 20% of the FAC effect at  $L = 10$ . Both of these issues will be addressed in future studies.

### 3.2. Plasmasphere

[28] The plasmopause, and/or dayside plume, and/or detached plasma are the favorable regions for EMIC wave generation in the inner magnetosphere. This is because the density gradient there is enhanced and counteracts refraction caused by the magnetic field gradient and curvature [e.g., *Horne and Thorne*, 1993; *Fraser et al.*, 2005; *Khazanov et al.*, 2006]. As a result, the net refraction is suppressed at the plasmopause/plume edge allowing wave packets to spend more time in the phase region of amplification. Thus, the cold plasma distribution is extremely crucial for EMIC wave excitation. Both the convection and the corotation electric fields control the cold plasma dynamics. As such, we will first present the snapshots of the total electric potential obtained from our simulations. Figure 6 shows the resulting equipotential contours, that also coincide with the instantaneous cold plasma flow. The most striking reconfiguration of the potential is observed in Figure 6 (middle and bottom) in the 28 and 30 hour snapshots. Referring to Figure 3, we see that starting at hour 28 the CPCP drop increases by about 100 kV during one hour for the W96 convection model. The strong convection causes a shrinking of the closed equipotential contours as shown in Figure 6 (there is stronger shrinking during hour 29). Later, an extremely developed SAPS is observed at hours 76–77 (see section 3.1), and the overshielding electric field (neg-

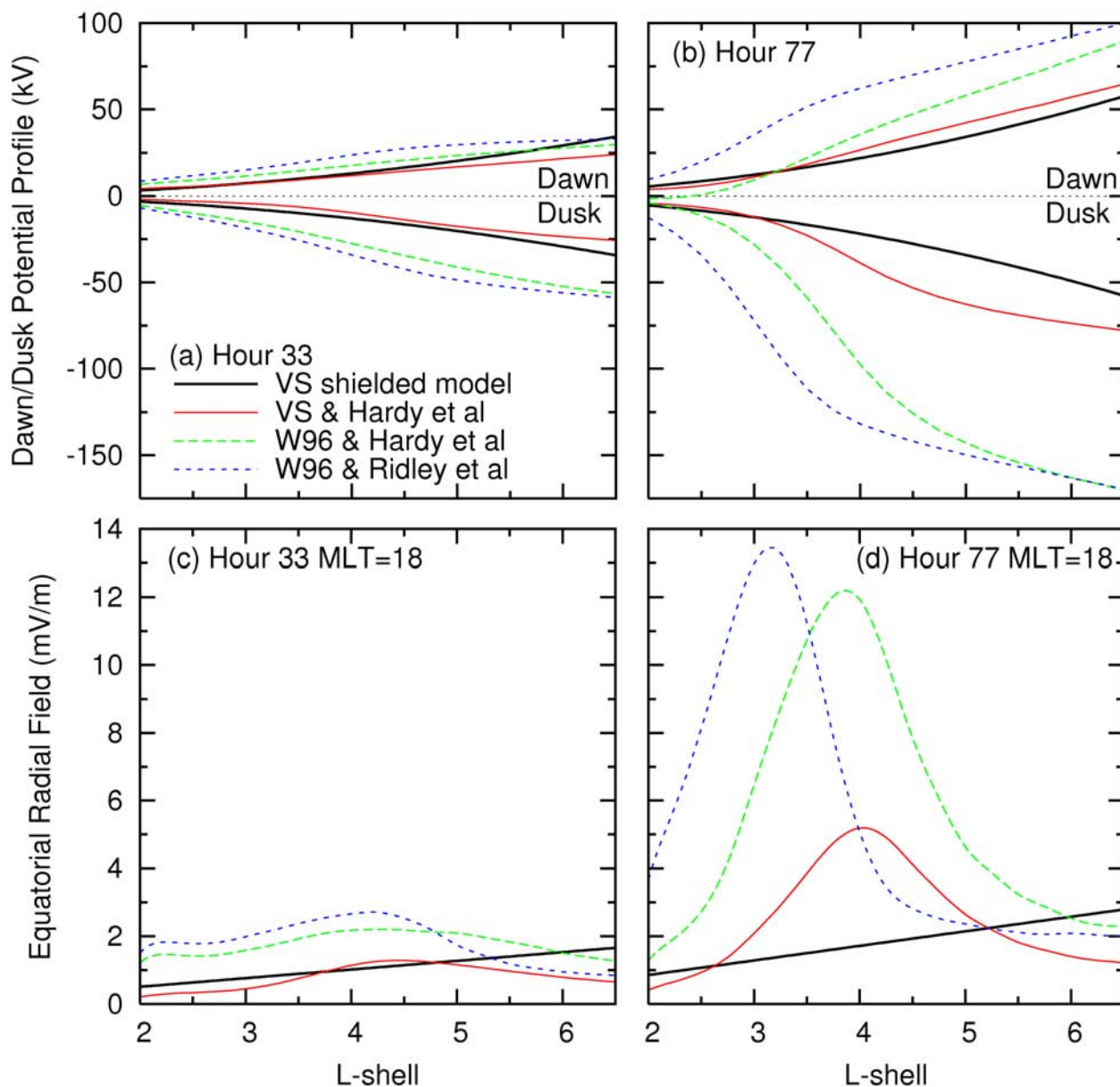


**Figure 5.** (a, b) The potential profiles on the dawn-dusk meridian, and (c, d) the equatorial radial electric field along MLT = 18 for hours 33 and 77.

ative  $E_y$ ) following a decrease of the CPCP difference in the W96 model is found in the inner magnetosphere at hour 79 (not shown).

[29] Figure 7 shows the selected distributions of the equatorial cold plasma density for three self-consistent simulations. For each run, the plasmasphere was first prepared by running the Ober code for 20 quiet days. Then, starting at 0000 UT on 1 May 1998, we solved the equations (1)–(10) using the initial and boundary conditions and the time series for all controlling parameters (see section 2.3). For the VS model (Figure 7, top), a broad dayside plume is formed a few hours before hour 28. Subsequently, up to hour 39 gradual intensification of the convection (see Figures 3 and 4) causes nightside plasmaspheric erosion and the plume narrowing in the MLT extent. The latter takes place mostly in the eastward flank of the plume where the convection and corotation fields

reinforce each other, while the duskside plume edge remains roughly stationary [Spasojević *et al.*, 2003; Goldstein *et al.*, 2005]. During the following storm progression, the magnetospheric convection field driven by the VS potential drop remains relatively high (see Figure 3), and the convection patterns are relatively steady (3-h cadence). Compared to Figure 7 (middle and bottom), these result in the most eroded and shrunken plasmasphere at hour 77 with a well defined nightside plasmapause (compare these results with Figure 7 in the work of Khazanov *et al.* [2006] where the entire plasmasphere was driven by the analytical formulation of the VS potential).

[30] Cold plasma density distributions in Figure 7 (middle and bottom) are qualitatively similar to each other, but exhibit quite a bit of difference compared to distributions in Figure 7 (top). At hour 28, the plasmasphere is well



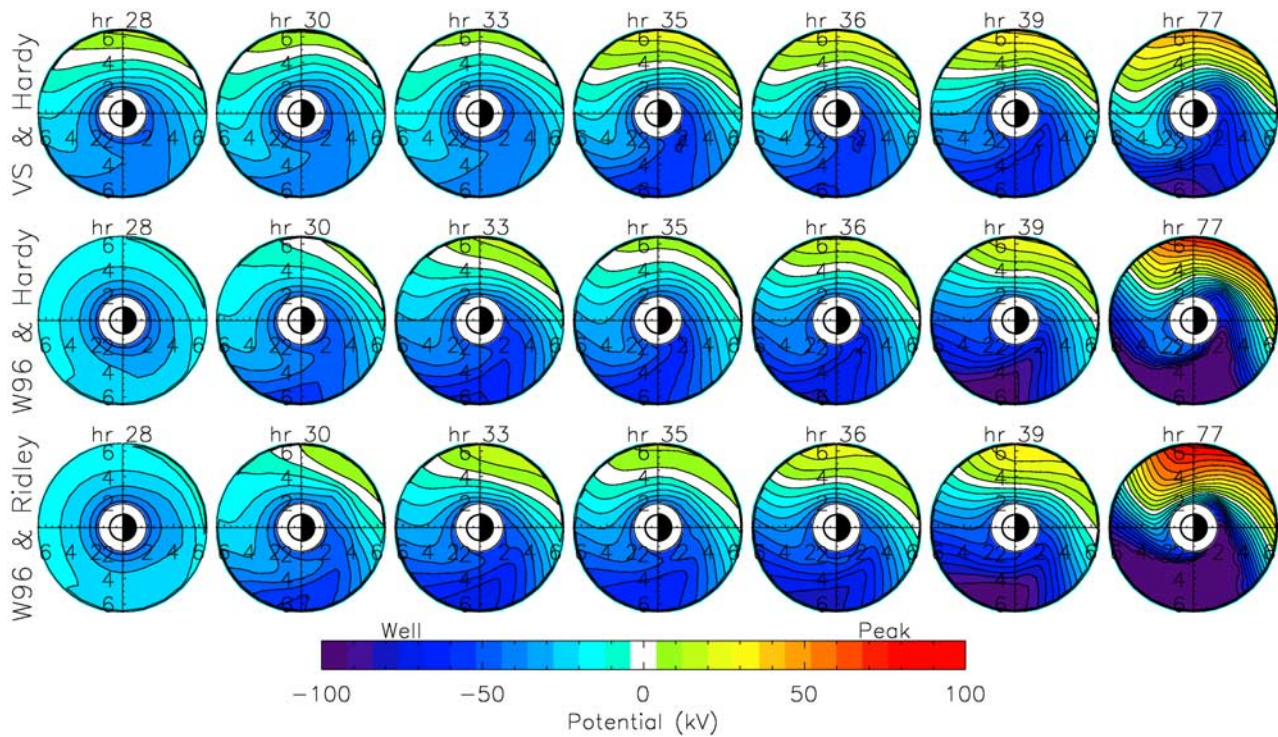


Figure 6. Same as Figure 4, except that the corotation field is included.

populated, and the plasmopause is well defined. Starting at hour 28, an increase of the CPCP drop by 100 kV during one hour (see Figure 3) causes formation of the plume by

hour 29 (not shown), and the presented snapshots at hour 30 are close to those at hour 29. One of the most distinguishable features observed in Figure 7 (middle and bottom) is

May 2–4, 1998: Thermal Plasma Density for VS & Hardy et al, W96 & Hardy et al, W96 & Ridley et al

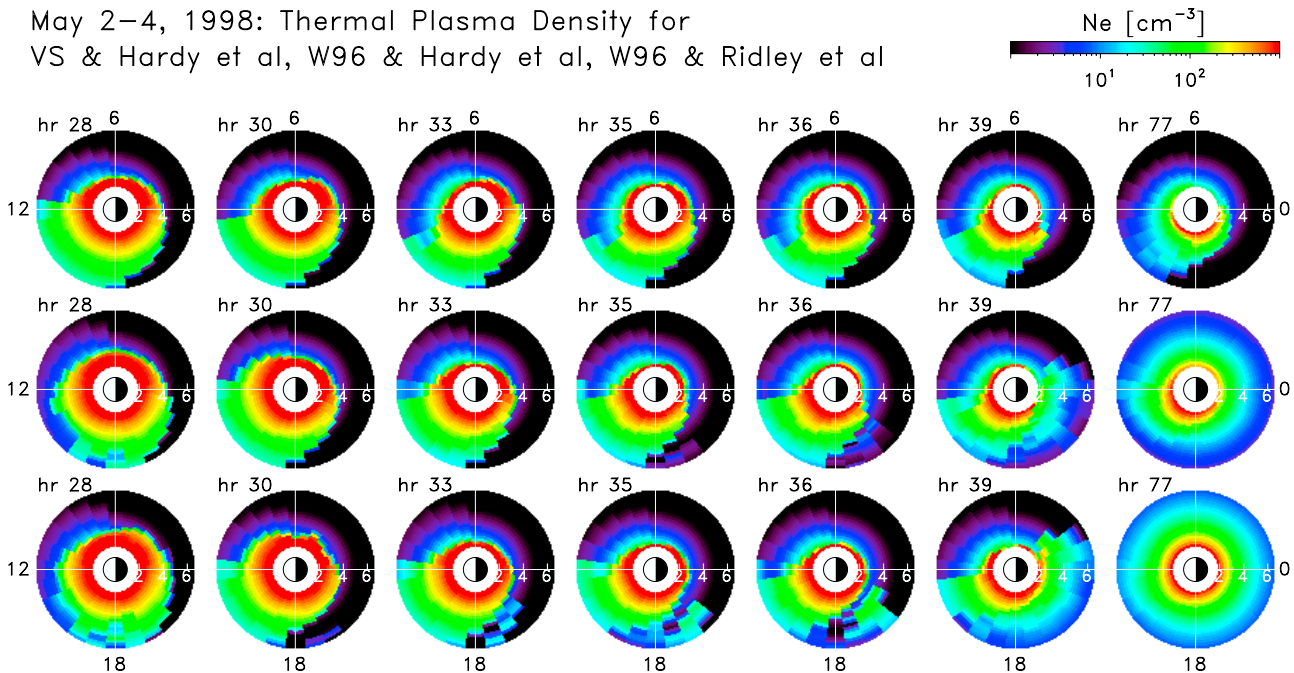
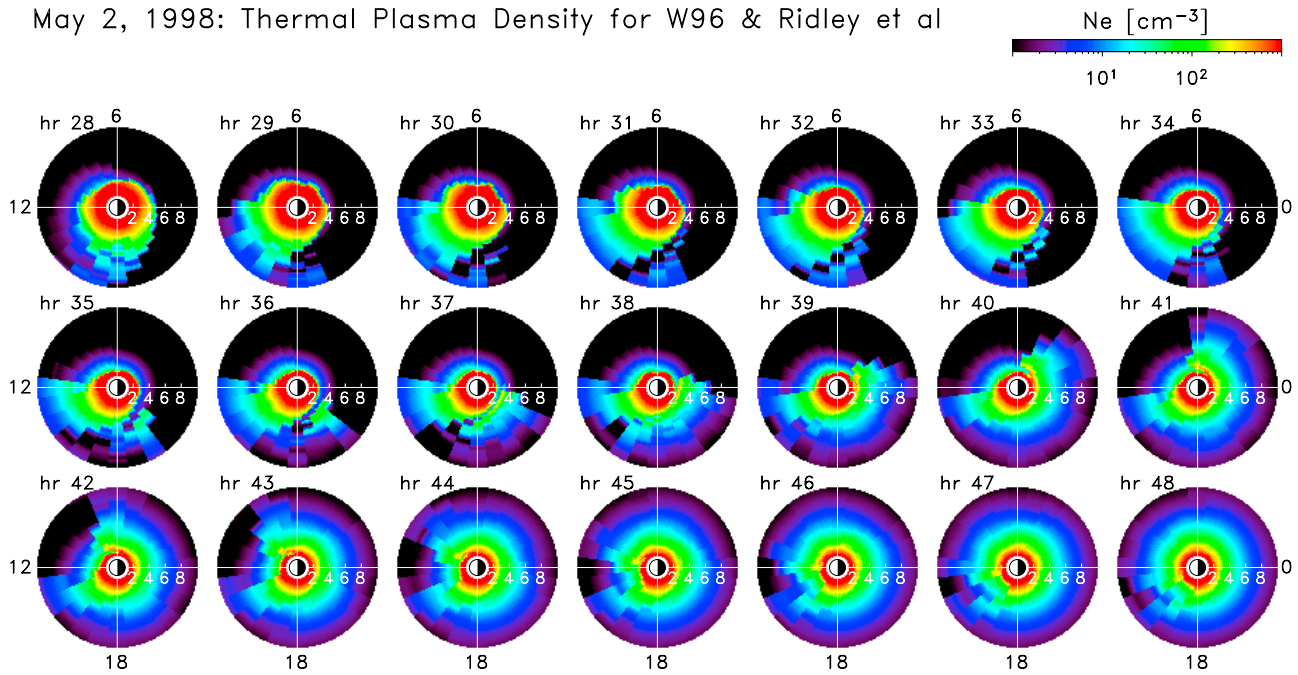


Figure 7. The equatorial cold plasma density distributions from three self-consistent simulations. (top) Results from a simulation with the VS model at the high latitude ionospheric boundary and the Hardy et al. conductance model. (middle) Simulation with the W96 model at  $\lambda = 69^\circ$  and the Hardy et al. conductance model. (bottom) The same as in Figure 7 (middle) except that the Ridley et al. empirical relationship between the FAC and conductance is used.



May 2, 1998: Thermal Plasma Density for W96 & Ridley et al



**Figure 8.** The equatorial cold plasma density distribution in the extended domain of  $L \leq 10$ . The electric field is specified by the W96 model above  $\lambda = 69^\circ$ , but it is calculated self-consistently below this latitude using the Ridley et al. relationship between the FAC and conductance.

the presence of a cold plasma on the nightside. To emphasize the existence of the recirculated detached plasma material, we show in Figure 8 the detailed plasma density evolution in the extended domain of  $L \leq 10$ . It is clearly seen in Figure 8 how this recirculated detached plasma is forming and reentering the inner magnetosphere. The radial electric field for MLT = 18 and 19 is also shown in Figure 9 for hours 28 and 29. The negative electric field in the outer region in Figure 9b is resulting in plasma recirculation. However, we have to emphasize that a great care is needed

to interpret these simulation results. During an extreme condition, the W96 model may predict a two-cell convection pattern with its focuses located at low latitude. The antisunward ionospheric plasma flow predicted by the W96 model may correspond to the lobe and the outer part of low-latitude boundary layer (LLBL) in the magnetosphere. In the dayside magnetosphere, when the plasmaspheric cold plasma is transported to LLBL, the cold plasma will flow in the antisunward direction [e.g., Ober et al., 1998]. At the same time, reentry of the cold plasma from LLBL back to

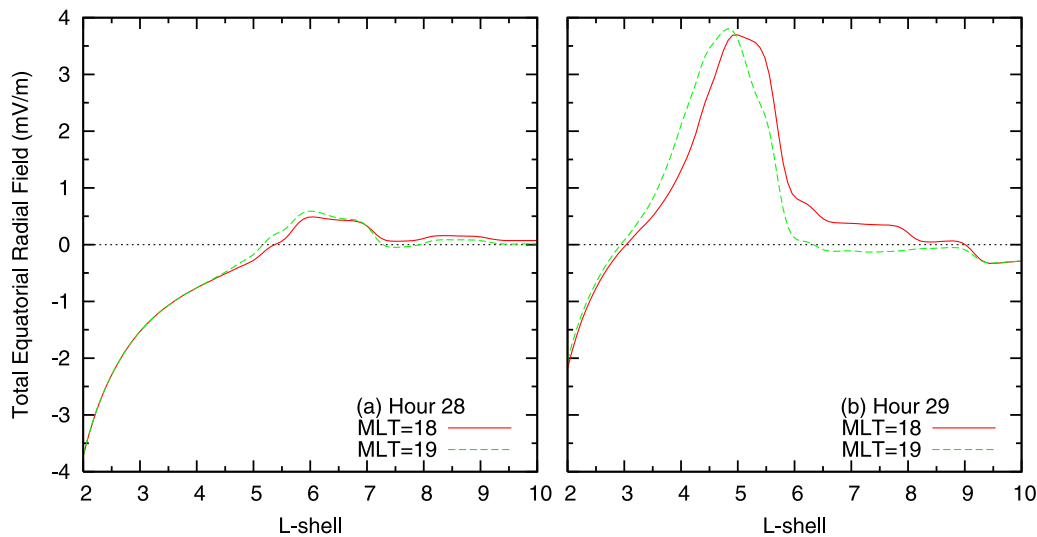


**Figure 9.** The total radial electric field (including the corotation field) in the equatorial plane. A combination of the W96 model and the Ridley et al. relationship was used to produce these results. Two profiles for MLT = 18 and 19 are shown for hours (a) 28 and (b) 29. The positive (negative) radial electric field is considered to be parallel (antiparallel) to the radius vector.

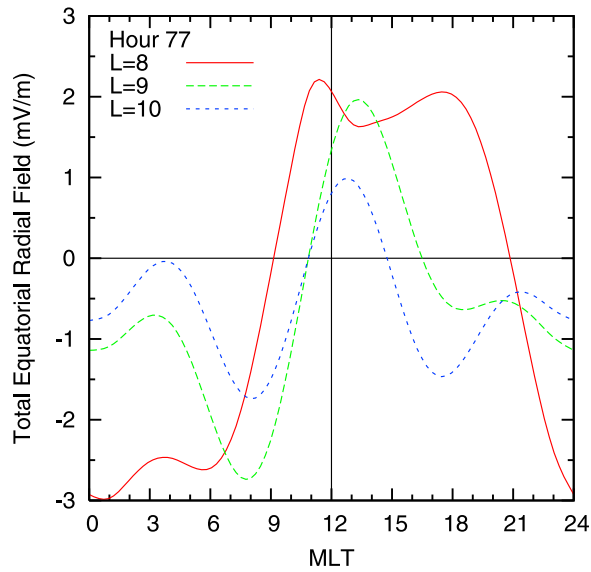


**Figure 10.** The total equatorial radial electric field versus MLT. A combination of the W96 model and the Ridley et al. relationship was used to produce these results. Three profiles for  $L = 8, 9,$  and  $10$  are shown for hour 77. The positive (negative) radial electric field is considered to be parallel (antiparallel) to the radius vector.

the magnetosphere may not be simple as predicted by the W96 model.

[31] Although the cold plasma recirculation is seen in both Figure 7 (middle) and Figure 7 (bottom), the observed similarity is only qualitative and all the quantitative characteristics are quite different. After hour 39, the W96 CPCP drop decreased and fluctuated around 50 kV except for four

hours on 4 May when the CPCP drop spikes to 300 kV during the second main phase of the storm (see Figure 3). In both cases, the resulting plasmaspheres at hour 77 are extremely diffusive with shallow density gradients. This is because the antisunward plasma flow is especially strong during the second main phase of the storm. To demonstrate that, we show in Figure 10 the total radial electric field versus MLT for  $L = 8, 9,$  and  $10$  at hour 77. The negative radial electric field in the afternoon-premidnight MLT sector causes a counter clockwise plasma convection. The MLT extent of the negative electric field in the afternoon-premidnight MLT sector grows with  $L$  shell, resulting in the backward plasma flow for  $MLT > 15$  at  $L = 10$ . This recirculation supplies the cold plasma in the nightside preventing the plasmasphere to be eroded. At the same time, as we emphasized above, a great care is needed to interpret these results.

[32] To show the equatorial cold plasma density profiles during the periods of a well defined and a shallow plasma-pause we selected hours 33 and 77. Results of our simulations are shown in Figure 11. We see a “classical” profile of the plasma-pause for hour 33, when the plasma density decreases about two orders of magnitude over  $0.5-0.75 R_E$ . The combination of the W96 model and the Ridley et al. relationship results in a detached plasma with a peak density of  $20 \text{ cm}^{-3}$ , which is clearly observed in Figure 11a (see also Figure 7, bottom). During hour 77, the plasmasphere driven by the VS CPCP drop is the most eroded and, although the plasmasphere boundary layer is wider than in Figure 11a and the plasma density drop is smaller, the plasma-pause is still well defined. For simulations with the W96 potential at the high latitude ionospheric boundary, both density profiles shown in Figure 11b exhibit a shallow density gradient without the plasma-pause while there is a clear change of the profile slope for the W96-Hardy et al. result. Note that there are also no steep density gradients outside of geostationary orbit (not shown).

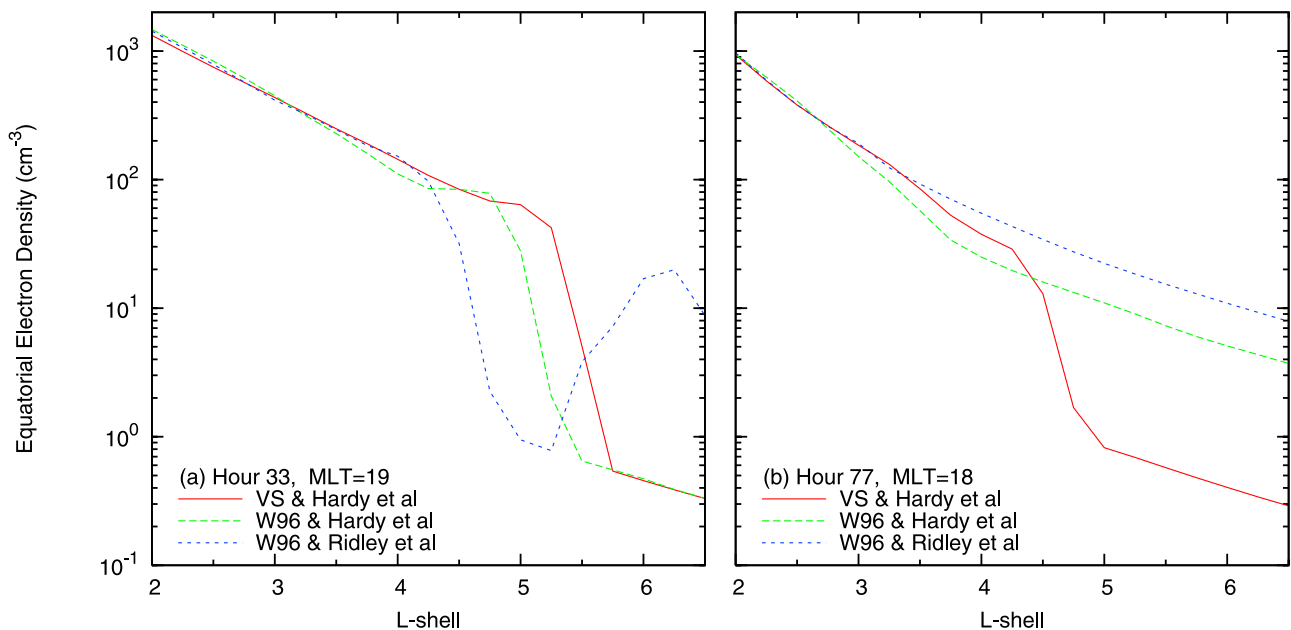


**Figure 11.** The equatorial cold plasma density versus  $L$  shell for hours (a) 33 and (b) 77. The profiles for hour 33 are plotted along  $MLT = 19$ , while the profiles for hour 77 are plotted along  $MLT = 18$ .

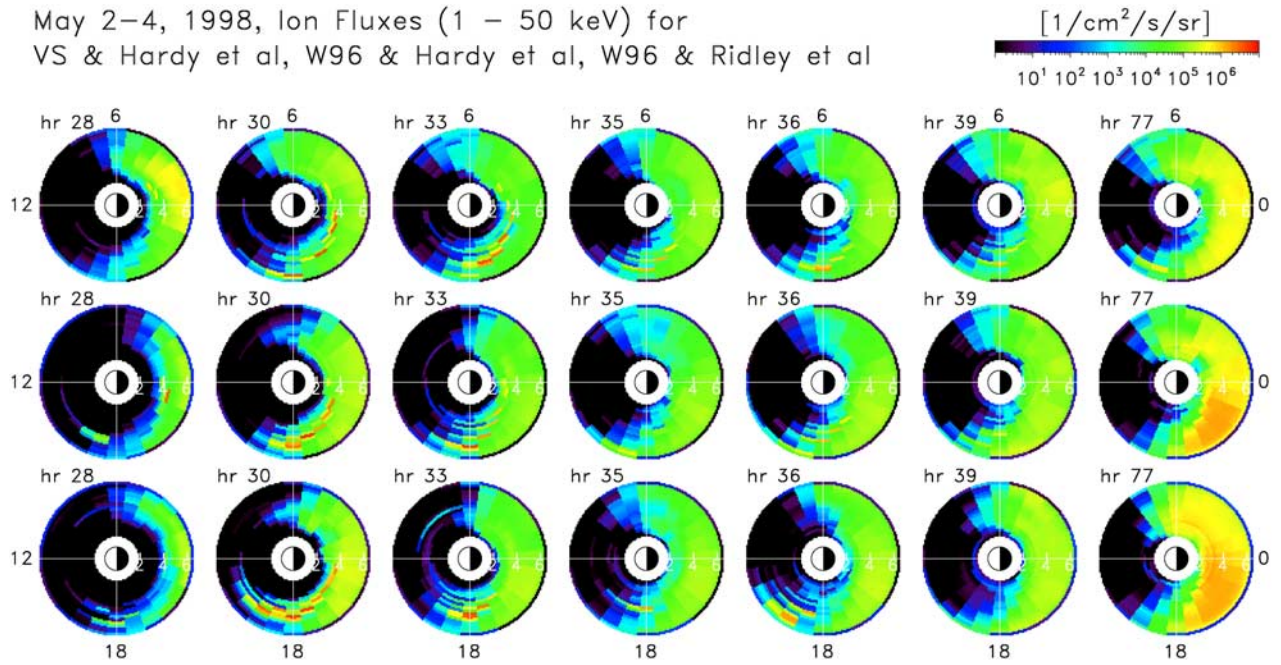


**Figure 12.** The RC proton precipitating fluxes averaged over the equatorial pitch angle loss cone and integrated over the energy range 1–50 keV.

### 3.3. RC Proton Precipitation

[33] The convection electric field controls the global precipitating patterns of RC. As RC protons approach the Earth via the convection electric field, they precipitate into the loss cone because the equatorial loss cone angle increases with decreasing L shell somewhat more than the equatorial pitch angle increases [e.g., *Jordanova et al.*, 1996]. Note that precipitation due to Coulomb collisions with thermal plasma takes place mainly inside the plasmasphere, and the wave-induced ion precipitation is organized in the radially narrow regions in the plasmasphere boundary layer [e.g., *Gurgiolo et al.*, 2005; *Khazanov et al.*, 2007b]. The RC proton precipitating fluxes integrated over two energy ranges 1–50 keV and 50–400 keV are calculated as

$$J_{lc} = \frac{1}{\Omega_{lc}} \int_{E_1}^{E_2} dE \int_{\mu_{lc}}^1 d\mu_0 j, \quad \Omega_{lc} = \int_{\mu_{lc}}^1 d\mu_0, \quad (11)$$

where  $\mu_{lc}$  is the cosine of the equatorial pitch angle at the boundary of the loss cone, and  $j$  is the equatorial differential flux of RC protons. The snapshots of the fluxes for low and high energies are shown in Figures 12 and 13, respectively. The results from three self-consistent runs with a specified combination of the high latitude ionospheric boundary potential and conductance model are shown. For low energy, the most intense precipitating fluxes near the end of the second main phase (hour 77) are observed in Figure 12 (middle and bottom) when the W96 model is used. This takes place because the convection field is strongest in these two cases (see Figure 4). The spot-like spatial structure in the postnoon-midnight MLT sector is due to the wave-induced precipitation with the strongest fluxes up to  $10^7 \text{ cm}^{-2} \text{ s}^{-1} \text{ sr}^{-1}$ .

[34] The penetrating electric field driven by the W96 boundary field causes precipitation of energetic RC ions well earthward of the low energy ion precipitation. It is clearly seen in Figure 13 that the W96 boundary potential leads to a strong precipitation of the high energy ions near the inner edge of RC during the second main phase on 4 May. The high energy precipitating fluxes maximize at about two times stronger magnitude than the maximal fluxes observed in the range 1–50 keV.

### 3.4. Energy Distribution for $\text{He}^+$ -Mode EMIC Waves

[35] The coupling of the magnetosphere and ionosphere by the region 2 FACs gives a self-consistent description of the magnetospheric electric field. This field controls the convective patterns of both RC ions and the cold plasmaspheric plasma, changing the conditions for EMIC wave generation/amplification. The equatorial (MLT, L shell) distribution of the squared wave magnetic field,

$$B_w^2(r_0, \varphi, t) = \int_{\omega_{\min}}^{\omega_{\max}} d\omega \int_0^\pi d\theta_0 B_w^2(r_0, \varphi, t, \omega, \theta_0),$$

is shown in Figure 14 for the  $\text{He}^+$ -mode EMIC waves. As before, the results from three self-consistent simulations are presented. Comparing Figure 14 with the cold plasma density distribution in Figure 7, we see that EMIC waves are distributed in the narrow regions inside the plasmasphere boundary layer where the density gradient is enhanced. Although, during hours 30–39, the spatial wave distributions in Figure 14 (top) and Figure 14 (middle) look similar, on average, there are much more waves in a simulation with the VS boundary condition than in a simulation with the W96 potential during entire 2 May. Moreover, there are practically no waves in the latter simulation after hour 39 (not shown) while in the former case we observe the



May 2–4, 1998, Ion Fluxes (50 – 400 keV) for  
 VS & Hardy et al, W96 & Hardy et al, W96 & Ridley et al

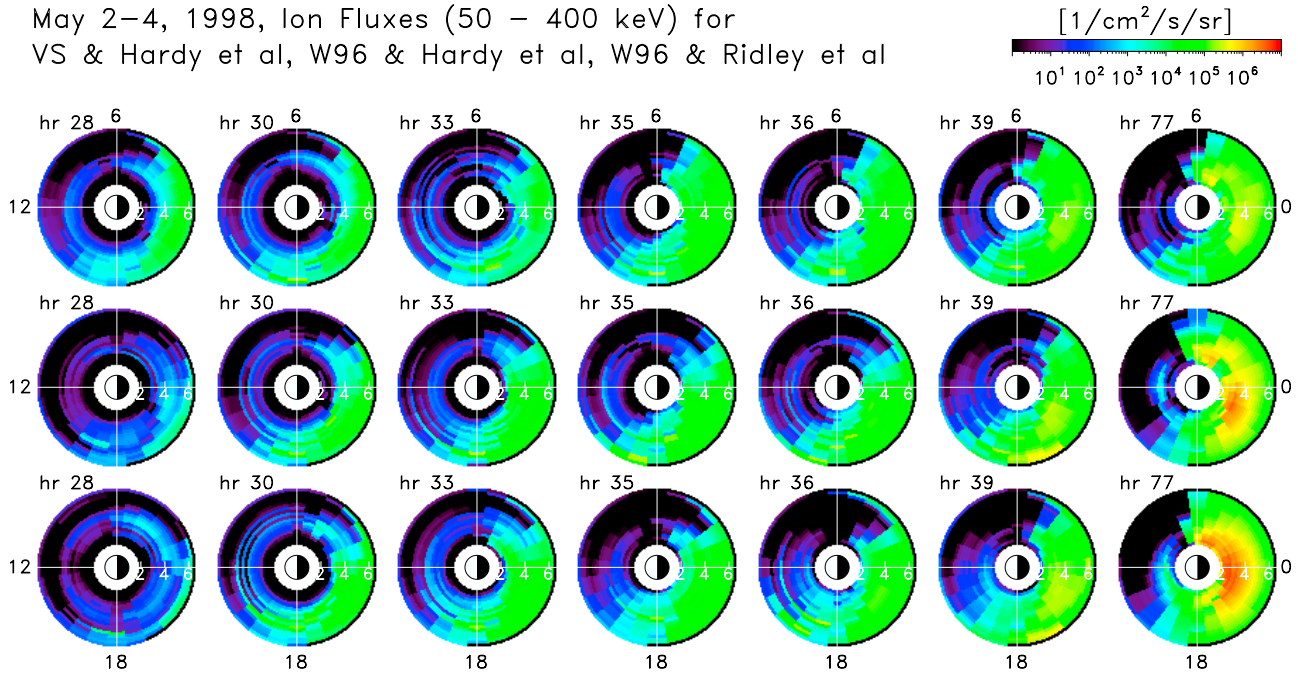


**Figure 13.** Same as Figure 12, except that the precipitating fluxes are integrated over the energy range 50–400 keV.

extended regions of intense waves during the majority of the time up to hour 60 (not shown). This is because the plasmapause is well defined and the CPCP drop is higher in the case of the VS potential boundary compared to the case of the W96 potential when the plasmasphere is highly

diffusive (a shallow density gradient) and RC is less intense (lower the local growth rate).

[36] The density distributions in Figure 7 (middle and bottom) demonstrate quite a bit of difference in the after-dusk MLT sector starting at hour 33. The plasmapause in

May 2–4, 1998, B-field Spectrogram for  
 VS & Hardy et al, W96 & Hardy et al, W96 & Ridley et al

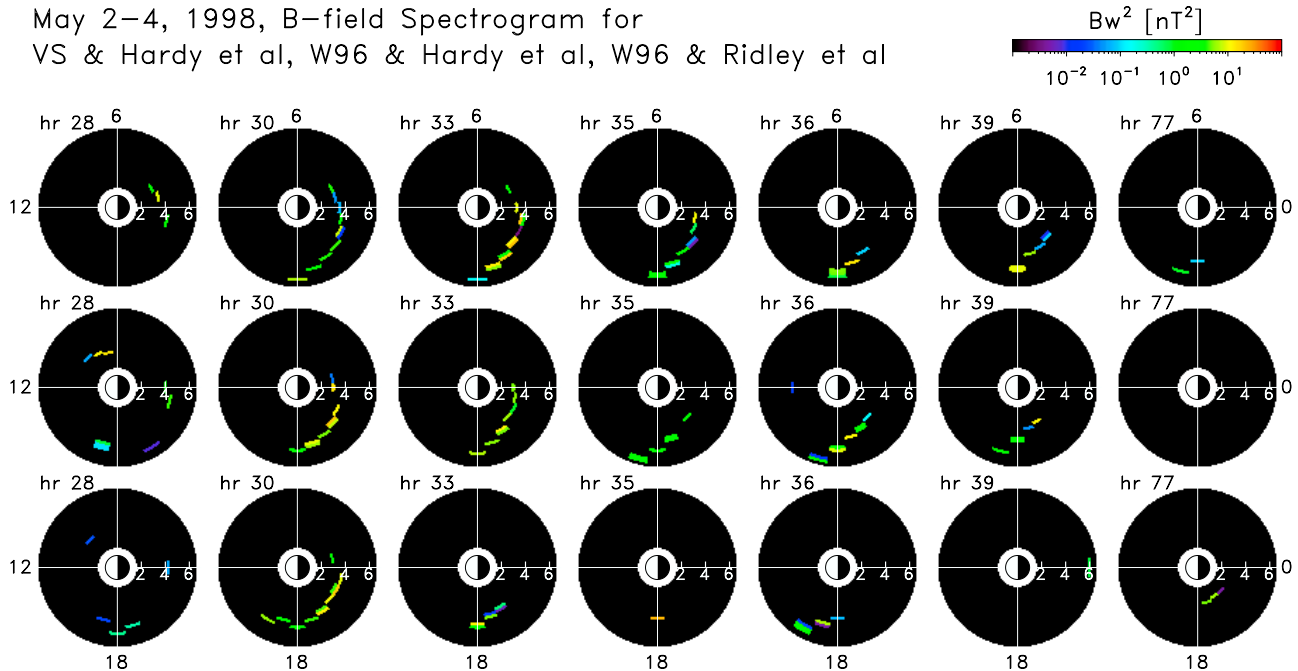


**Figure 14.** The distributions of squared wave magnetic field for the  $He^+$ -mode EMIC waves. (top) Results from a simulation with the VS model at the high latitude ionospheric boundary and the Hardy et al. conductance model. (middle) Simulation with the W96 model at the ionospheric boundary and the Hardy et al. conductance model. (bottom) The same as in Figure 14 (middle) except that the Ridley et al. empirical relationship between the FAC and conductance is used.

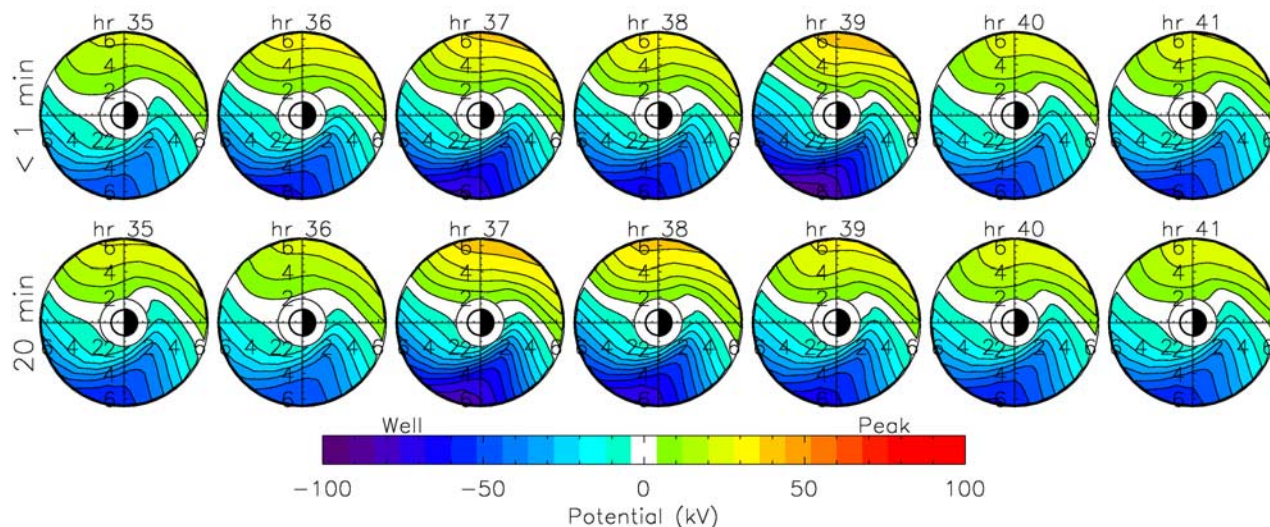


**Figure 15.** The equatorial potential contours in the inner magnetosphere without a corotation field. The view is over the North Pole with local noon to the left. All of the results are from simulations with the W96 potential at the high latitude ionospheric boundary and use the Hardy et al. conductance model. (top) The magnetospheric electric field is updated each minute in accordance with the instantaneous interplanetary conditions (a 30-min time delay is applied) and FACs. (bottom) The interplanetary parameters and FACs are averaged over a 20-min window prior to sending them to the ionospheric solver, and the magnetospheric electric field is updated once every 20 min. Equipotentials are drawn every 8 kV.

Figure 7 (bottom) is located closer to the Earth, and the density gradient is shallowed by the detached plasma. At the same time, we observe much less wave activity in Figure 14 (bottom) than in Figure 14 (middle). This is likely due to the effect of the density distribution, because the global potential drop is even higher in Figure 4 (bottom) (suggesting a more intense RC) compared to Figure 4 (middle).

[37] There are practically no waves during the second main and recovery phases, except for moderate wave activity in the hour 77 snapshots in Figure 14 (top and bottom). In the case of the VS-Hardy et al. combination, the plasmapause is well defined during hour 77 (see Figures 7 and 11) and waves can grow despite a less intense RC in this case. On the other hand, the RC is strongly developed for the case of the W96 potential, and wave growth rate is essentially higher than in Figure 14 (top), causing a wave generation despite the plasmasphere being extremely diffuse and the density gradient being shallow.

### 3.5. Ionosphere Reconfiguration and Communication Time

[38] All of the results presented above were obtained from simulations when only a 30-min time delay between WIND and the high latitude ionospheric boundary was applied. Both the reconfiguration time needed to reestablish a new potential pattern throughout the ionosphere and communication time between the ionosphere and the equatorial magnetosphere were assumed to be zero. These allowed us to update the equatorial electric field for each time step (a minute). However, this is not the case and both the ionospheric reconfiguration time and the Alfvén propagation time are essentially higher than a minute [e.g., Ridley et al., 1998]. This implies that the ionosphere cannot reconfigure instantly in response to change of the interplan-

etary conditions, and that the magnetospheric electric field requires a finite time to be reestablished.

[39] Ridley et al. [1998] studied the ionospheric convection changes associated with changes of the IMF. They found that the total reconfiguration time of the ionosphere is in the range 3–26 min with an average of 13 min. Taking 7 min as a typical communication time between the ionosphere and the equatorial magnetosphere (for example, the magnetopause-ionosphere communication time is  $8.4 \pm 8.2$  min as estimated by Ridley et al. [1998]), on average, the same 13 min are needed to reestablish a new potential pattern in the magnetosphere but a 7 min delay should be applied to the ionospheric pattern. Because a great deal of scatter was reported for both time scales, below we simply adopt 20 (= 13 + 7) min as a time needed to reestablish a new potential pattern in the equatorial magnetosphere.

[40] To assess the importance of the finite ionospheric reconfiguration and communication time effect, we reran the “W96-Hardy et al.” simulation. Starting at hour 24, we averaged the interplanetary parameters and FACs over a 20-min window before passing them to the ionospheric solver, and updated the equatorial electric field only once every 20 min. Figure 15 shows the equatorial potential contours from this simulation along with the contours from the previous simulation, when the equatorial electric field is updated for each time step. The results during seven consecutive hours are shown (hours 35–41). The potential distributions in Figure 15 (top and bottom) are quite a bit different suggesting that the finite ionospheric reconfiguration and communication time effect may be important, especially for the fine temporal-spatial structure of the plasmasphere-magnetosphere system. Although the “new” electric field alters the RC, wave, and cold plasma distributions, we show only the results for cold plasma density.

May 2–4, 1998: Thermal Plasma Density for  
Instant E–field reconfig, and 20 min reconfig time

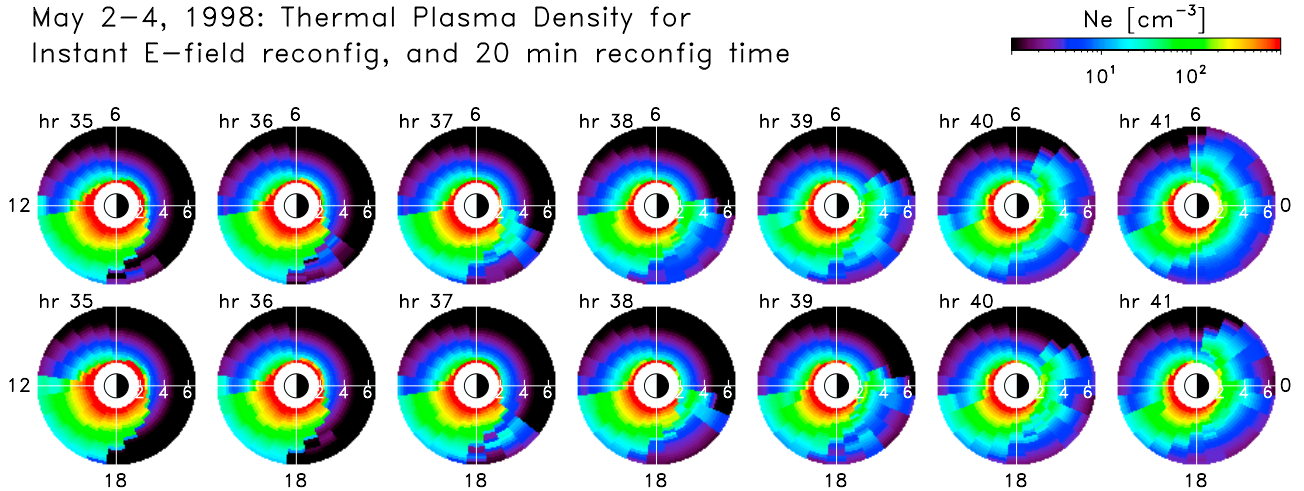


**Figure 16.** The equatorial cold plasma density distributions from simulations with the W96 potential at the high latitude ionospheric boundary and the Hardy et al. conductance model. (top) The magnetospheric electric field is updated each minute accordingly to the instantaneous interplanetary conditions (with a 30-min time delay) and FACs. (bottom) The interplanetary parameters and FACs are averaged over a 20-min window prior to sending them to the ionospheric solver and the magnetospheric electric field is updated once every 20 min.

Figure 16 demonstrates a difference in the cold plasma density distribution introduced by the effect of a finite time required to reestablish a “new” distribution of the magnetospheric electric field. Although the density distributions in these two simulations are identical at hour 24, the plasma-pause/plume shapes get a visible difference in the dawn-noon MLT sector starting at hour 29 (not shown). Later, starting at hour 35, an essential difference between the density distributions is observed in the night MLT sector (see Figure 16). After hour 56, the cold plasma density distributions in these two simulations are similar. This is expected after a long-term interval of system evolution, while the fine density structure still differs from time to time depending on the differences in the electric field distributions in these two simulations.

[41] Although a more sophisticated methodology is required to treat and separate the effects of the finite ionospheric reconfiguration and communication time, Figures 15 and 16 clearly demonstrate that the finite time effect is important, especially for the fine temporal-spatial structure of the system. This implies that the instant interplanetary parameters cannot be used in order to specify the outer ionospheric boundary condition, but rather some kind of the averaging procedure should be applied to these parameters before passing them to the ionospheric solver.

#### 4. Summary

[42] The scattering rate of magnetospheric RC ions and relativistic electrons by EMIC waves is not only controlled by the wave intensity-spatial-temporal distribution but strongly depends on the spectral distribution of the wave power. There is growing experimental [Anderson et al., 1996; Denton et al., 1996; Anderson et al., 1992b; Fraser and Nguyen, 2001; Meredith et al., 2003] and theoretical [Horne and Thorne, 1993; Khazanov et al., 2006; Khazanov and Gamayunov, 2007] evidence that EMIC waves can be highly oblique in the Earth’s magnetosphere. Compared to

field-aligned waves, the highly oblique wave normal angle distributions can dramatically change the effectiveness (an order of magnitude or more) of both the RC proton precipitation [Khazanov et al., 2007b] and relativistic electron scattering [Glauert and Horne, 2005; Khazanov and Gamayunov, 2007]. Strong sensitivity of the scattering rates to the wave spectral characteristics suggests that in any effort to model EMIC wave-induced heating and/or scattering of the magnetospheric particles, the wave spectral distribution requires special care and should be properly established. Unfortunately, there are still very few satellite-based studies of EMIC waves, especially during the main phase of magnetic storms, and currently available observational information regarding EMIC wave power spectral density is poor [Engebretson et al., 2008]. So, a combination of comprehensive theoretical models and available data should be utilized to obtain the power spectral density of EMIC waves on the global magnetospheric scale throughout the different storm phases. To the best of our knowledge, there is only one model that is able to simulate a spatial, temporal and spectral distribution of EMIC waves on the global magnetospheric scale during the different storm phases [Gamayunov and Khazanov, 2008]. This model is based on first principles and is governed by a coupled system of the RC kinetic equation and the wave kinetic equation, explicitly including the wave generation/damping, propagation, refraction, reflection and tunneling in a multi-ion magnetospheric plasma.

[43] The convective patterns of both the RC ions and the cold plasmaspheric plasma are controlled by the magnetospheric electric field, thereby determining the conditions for interaction of RC ions and EMIC waves. Therefore, this electric field is one of the most crucial elements in simulating the wave power spectral density on a global magnetospheric scale. Self-consistent simulation of the magnetosphere-ionosphere system should provide, at least in principle, the most accurate theoretical electric field [Vasyliunas, 1970; Jaggi and Wolf, 1973]. The need for a self-consistent model



of the magnetospheric electric field, RC, plasmasphere, and EMIC waves is evident. In the present study we have incorporated the large scale magnetosphere-ionosphere electrodynamic coupling in our previous self-consistent model of interacting RC ions and EMIC waves [Gamayunov and Khazanov, 2008]. The resulting computational model treats self-consistently not only EMIC waves and RC ions but also the magnetospheric electric field, RC, and plasmasphere.

[44] A few runs of this new model were performed to get a qualitative assessment of the effects of the high latitude ionospheric boundary condition and the ionospheric conductance. The results presented in this study were obtained from simulations of the 2–4 May 1998 geomagnetic storm (mostly the 2–3 May period). We have performed three simulations that differ by the electric potential specified at the high latitude ionospheric boundary (we used the W96 model and the VS model with  $Kp$  parameterization), and/or the ionospheric conductance from auroral precipitation (utilizing the Hardy et al. conductance model and the Ridley et al. relationship between the FACs and the conductance). The following three combinations have been used in the simulations: (1) the VS model and the Hardy et al. model; (2) the W96 model and the Hardy et al. model; and (3) the W96 model and the Ridley et al. relationship. In addition, one more simulation has been done: (4) the W96 model and the Hardy et al. model applying a 20-min window as the time needed to reestablish a new potential pattern in the magnetosphere. The RC in the present study has been simulated inside geostationary orbit only, and the high latitude ionospheric boundary has been placed near the ionospheric projection of this orbit. The findings from our initial consideration can be summarized as follows:

[45] 1. Although the poleward boundary for the ionospheric potential is specified at the projection of geostationary orbit in most models (probably except the Rice Convection Model), we are not able to specify well the ionospheric potential there. Indeed, the existing models of ionospheric electric potential (like the AMIE technique [Richmond and Kamide, 1988], the Weimer [1996, 2001] and the Boyle et al. [1997] models) are much more reliable at high latitudes and give a poor representation of the potential and its significant variation in the inner magnetosphere [Foster and Vo, 2002]. In addition, the effect of FACs is proportional to the volume of the magnetic flux tube, and so this effect at  $L = 6.6$  is about 20% of the FAC effect at  $L = 10$ , suggesting that FACs beyond geostationary orbit may produce a major shielding of midlatitudes from a high latitude driving field. So the region beyond geostationary orbit should be included in the magnetosphere-ionosphere coupling. An extension of the simulation domain, at least to  $\lambda = 72^\circ$ , is vital for a truly self-consistent modeling of the magnetosphere-ionosphere coupling.

[46] 2. Compared to the case of the Hardy et al. model, the Ridley et al. empirical relationship between the FAC and conductance produces quite a bit of difference in the potential distribution and, overall, stronger convection at the subauroral latitudes (see Figures 4 and 5). This difference strongly affects the cold plasma distribution, RC precipitation pattern, and EMIC waves (see Figures 7, 11, 12, 13, and 14). More importantly, a self-consistent description of the ionospheric conductance makes equation (9)

nonlinear compared to the case of a statistical conductance model. This is a principle point requiring that a self-consistent model, based on first principles, of the ionospheric conductance should be incorporated into a simulation of the magnetosphere-ionosphere coupling.

[47] 3. A fine density structure in the plasmasphere boundary layer, plume, detached plasma etc. controls the wave propagation. This fine structure may be a more crucial factor in controlling the generation of EMIC waves, than just the intensity/distribution of the RC and the local plasma density. There is very large difference between the wave activity in Figure 14 (middle) and Figure 14 (bottom) while the density distributions in Figure 7 (middle and bottom) do not differ so dramatically. This suggests that to model the EMIC wave distribution and wave spectral properties accurately, the plasmasphere should be simulated self-consistently because its fine structure requires as much care as that of the RC.

[48] 4. It is shown that the effect of a finite time needed to reestablish a new potential pattern throughout the ionosphere and to communicate between the ionosphere and the equatorial magnetosphere is important. This effect was ignored in all previous simulations but it should be taken into account to model a self-consistent electric field properly.

[49] Concluding we would like to emphasize that in order to make significant progress in developing a truly self-consistent model of the electric field, we need to considerably improve our ability to accurately specify the electric field at high latitudes and ionospheric conductance. Without this ability, we will not be able to accurately specify EMIC wave spectra in the inner magnetosphere and correctly describe the wave-induced heating and/or scattering of the magnetospheric particles.

[50] **Acknowledgments.** We would like to thank M. Thomsen for providing LANL data. The solar wind magnetic field and plasma data are obtained from the CDAWeb maintained by the MFI team (R. Lepping, PI) and the SWE team (K. Ogilvie, PI) of the Wind satellite. We thank D. Ober for providing the code of the dynamic global core plasma model. Funding in support of this study was provided by NASA grant UPN 370–16–10, NASA HQ POLAR Project, and the NASA LWS Program.

[51] Zuyin Pu thanks the reviewers for their assistance in evaluating this paper.

## References

- Ahn, B.-H., A. D. Richmond, Y. Kamide, H. W. Kroehl, B. A. Emery, O. de la Beaujardière, and S.-I. Akasofu (1998), An ionospheric conductance model based on ground magnetic disturbance data, *J. Geophys. Res.*, *103*, 14,769.
- Akhiezer, A. I., I. A. Akhiezer, R. V. Polovin, A. G. Sitenko, and K. N. Stepanov (1975), *Plasma Electrodynamics*, vol. 2, Pergamon, Tarrytown, N. Y.
- Albert, J. M. (2003), Evaluation of quasi-linear diffusion coefficients for EMIC waves in a multispecies plasma, *J. Geophys. Res.*, *108*(A6), 1249, doi:10.1029/2002JA009792.
- Amm, O. (1996), Comment on “A three-dimensional, iterative mapping procedure for the implementation of an ionosphere-magnetosphere anisotropic Ohm’s law boundary condition in global magnetohydrodynamic simulations”, *Ann. Geophys.*, *14*, 773.
- Anderson, B. J., and S. A. Fuselier (1994), Response of thermal ions to electromagnetic ion cyclotron waves, *J. Geophys. Res.*, *99*, 19,413.
- Anderson, B. J., R. E. Erlandson, and L. J. Zanetti (1992a), A statistical study of Pc 1–2 magnetic pulsations in the equatorial magnetosphere, 1, Equatorial occurrence distributions, *J. Geophys. Res.*, *97*, 3075.
- Anderson, B. J., R. E. Erlandson, and L. J. Zanetti (1992b), A statistical study of Pc 1–2 magnetic pulsations in the equatorial magnetosphere, 2, Wave properties, *J. Geophys. Res.*, *97*, 3089.
- Anderson, B. J., R. E. Denton, and S. A. Fuselier (1996), On determining polarization characteristics of ion cyclotron wave magnetic field fluctuations, *J. Geophys. Res.*, *101*, 13,195.

- Anderson, P. C., R. A. Heelis, and W. B. Hanson (1991), Ionospheric signatures of rapid subauroral ion drifts, *J. Geophys. Res.*, *96*, 5785.
- Anderson, P. C., W. R. Hanson, E. A. Heelis, J. D. Craven, D. N. Baker, and L. A. Frank (1993), A proposed production model of rapid subauroral ion drifts and their relationship to substorm evolution, *J. Geophys. Res.*, *98*, 6069.
- Angerami, J. J., and J. O. Thomas (1964), Studies of planetary atmospheres, 1, The distribution of ions and electrons in the earth's exosphere, *J. Geophys. Res.*, *69*, 4537.
- Bame, S. J., et al. (1993), Magnetospheric plasma analyzer for spacecraft with constrained resources, *Rev. Sci. Instrum.*, *64*, 1026.
- Belian, R. D., G. R. Gislser, T. Cayton, and R. Christensen (1992), High-Z energetic particles at geosynchronous orbit during the great solar proton event series of October 1989, *J. Geophys. Res.*, *97*, 16,897.
- Bezrukhikh, V. V., and K. I. Gringauz (1976), The hot zone in the outer plasmasphere of the Earth, *J. Atmos. Terr. Phys.*, *38*, 1085.
- Boyle, C. B., P. H. Reiff, and M. R. Hairston (1997), Empirical polar cap potentials, *J. Geophys. Res.*, *102*, 111.
- Bräysy, T., K. Mursula, and G. Marklund (1998), Ion cyclotron waves during a great magnetic storm observed by Freja double-probe electric field instrument, *J. Geophys. Res.*, *103*, 4145.
- Burke, W. J., T. L. Fehrer, D. R. Weimer, C. Y. Huang, M. S. Gussenhoven, F. J. Rich, and L. C. Gentile (1998), Observed and predicted potential distributions during the October 1995 magnetic cloud passage, *Geophys. Res. Lett.*, *25*, 3023.
- Chamberlain, J. W. (1963), Planetary corona and atmospheric evaporation, *Planet. Space Sci.*, *11*, 901.
- Cornwall, J. M. (1965), Cyclotron instabilities and electromagnetic emission in the ultra low frequency and very low frequency ranges, *J. Geophys. Res.*, *70*, 61.
- Cornwall, J. M., F. V. Coroniti, and R. M. Thorne (1970), Turbulent loss of ring current protons, *J. Geophys. Res.*, *75*, 4699.
- Cornwall, J. M., F. V. Coroniti, and R. M. Thorne (1971), Unified theory of SAR arc formation at the plasmapause, *J. Geophys. Res.*, *76*, 4428.
- Daglis, I. A. (1997), The role of magnetosphere-ionosphere coupling in magnetic storm dynamics, in *Magnetic Storms*, *Geophys. Monogr. Ser.*, vol. 98, edited by B. T. Tsurutani, W. D. Gonzalez, Y. Kamide, and J. K. Arballo, p. 107, AGU, Washington, D. C.
- Denton, R. E., B. J. Anderson, G. Ho, and D. C. Hamilton (1996), Effects of wave superposition on the polarization of electromagnetic ion cyclotron waves, *J. Geophys. Res.*, *101*, 24,869.
- Ebihara, Y., M.-C. Fok, R. A. Wolf, T. J. Immel, and T. E. Moore (2004), Influence of ionospheric conductivity on the ring current, *J. Geophys. Res.*, *109*, A08205, doi:10.1029/2003JA010351.
- Engebretson, M. J., M. R. Lessard, J. Bortnik, J. C. Green, R. B. Horne, D. L. Detrick, A. T. Weatherwax, J. Manninen, N. J. Petit, J. L. Posch, and M. C. Rose (2008), Pc1–Pc2 waves and energetic particle precipitation during and after magnetic storms: Superposed epoch analysis and case studies, *J. Geophys. Res.*, *113*, A01211, doi:10.1029/2007JA012362.
- Erlanson, R. E., and A. J. Ukhorskiy (2001), Observations of electromagnetic ion cyclotron waves during geomagnetic storms: Wave occurrence and pitch angle scattering, *J. Geophys. Res.*, *106*, 3883.
- Erlanson, R. E., L. J. Zanetti, T. A. Potemra, L. P. Block, and G. Holmgren (1990), Viking magnetic and electric field observations of Pc 1 waves at high latitudes, *J. Geophys. Res.*, *95*, 5941.
- Fang, X., M. W. Liemohn, and J. U. Kozyra (2007a), Global 30–240 keV proton precipitation in the 17–18 April 2002 geomagnetic storms: 2. Conductances and beam spreading, *J. Geophys. Res.*, *112*, A05302, doi:10.1029/2006JA012113.
- Fang, X., A. J. Ridley, M. W. Liemohn, J. U. Kozyra, and D. S. Evans (2007b), Global 30–240 keV proton precipitation in the 17–18 April 2002 geomagnetic storms: 3. Impact on the ionosphere and thermosphere, *J. Geophys. Res.*, *112*, A07310, doi:10.1029/2006JA012144.
- Farrugia, C. J., et al. (2003), Large-scale geomagnetic effects of May 4, 1998, *Adv. Space Res.*, *31*(4), 1111.
- Foat, J. E., R. P. Lin, D. M. Smith, F. Fenrich, R. Millan, I. Roth, K. R. Lorentzen, M. P. McCarthy, G. K. Parks, and J. P. Treilhou (1998), First detection of a terrestrial MeV X-ray burst, *Geophys. Res. Lett.*, *25*, 4109.
- Fok, M.-C., J. U. Kozyra, A. F. Nagy, C. E. Rasmussen, and G. V. Khazanov (1993), A decay model of equatorial ring current and the associated aeronomical consequences, *J. Geophys. Res.*, *98*, 19,381.
- Fok, M.-C., R. A. Wolf, R. W. Spiro, and T. E. Moore (2001), Comprehensive computational model of Earth's ring current, *J. Geophys. Res.*, *106*, 8417.
- Foster, J. C., and W. J. Burke (2002), SAPS: A new categorization for subauroral electric fields, *Eos Trans. AGU*, *83*(36), 393.
- Foster, J. C., and H. B. Vo (2002), Average characteristics and activity dependence of the subauroral polarization stream, *J. Geophys. Res.*, *107*(A12), 1475, doi:10.1029/2002JA009409.
- Fraser, B. J., and T. S. Nguyen (2001), Is the plasmapause a preferred source region of electromagnetic ion cyclotron waves in the magnetosphere?, *J. Atmos. Sol. Terr. Phys.*, *63*, 1225.
- Fraser, B. J., H. J. Singer, M. L. Adrian, D. L. Gallagher, and M. F. Thomsen (2005), The relationship between plasma density structure and EMIC waves at geosynchronous orbit, in *Inner Magnetosphere Interactions: New Perspectives from Imaging*, *Geophys. Monogr. Ser.*, vol. 159, edited by J. L. Burch, M. Schulz, and H. Spence, p. 55, AGU, Washington, D. C.
- Fuselier, S. A., and B. J. Anderson (1996), Low-energy  $He^+$  and  $H^+$  distributions and proton cyclotron waves in the afternoon equatorial magnetosphere, *J. Geophys. Res.*, *101*, 13,255.
- Galand, M., and A. D. Richmond (2001), Ionospheric electrical conductances produced by auroral proton precipitation, *J. Geophys. Res.*, *106*, 117.
- Galand, M., R. G. Roble, and D. Lummerzheim (1999), Ionization by energetic protons in Thermosphere-Ionosphere Electrodynamics General Circulation Model, *J. Geophys. Res.*, *104*, 27,973.
- Galand, M., T. J. Fuller-Rowell, and M. V. Codrescu (2001), Response of the upper atmosphere to auroral protons, *J. Geophys. Res.*, *106*, 127.
- Galeev, A. A. (1975), Plasma turbulence in the magnetosphere with special regard to plasma heating, in *Physics of the Hot Plasma in the Magnetosphere*, edited by B. Hultquist and L. Stenflo, p. 251, Plenum, New York.
- Gamayunov, K. V., and G. V. Khazanov (2008), Crucial role of ring current  $H^+$  in electromagnetic ion cyclotron wave dispersion relation: Results from global simulations, *J. Geophys. Res.*, *113*, A11220, doi:10.1029/2008JA013494.
- Garcia, H. A., and W. N. Spjeldvik (1985), Anisotropy characteristics of geomagnetically trapped ions, *J. Geophys. Res.*, *90*, 347.
- Garner, T. W., R. A. Wolf, R. W. Spiro, W. J. Burke, B. G. Fejer, S. Sazykin, J. L. Roeder, and M. R. Hairston (2004), Magnetospheric electric fields and plasma sheet injection to low L shells during the 4–5 June 1991 magnetic storm: Comparison between the Rice Convection Model and observations, *J. Geophys. Res.*, *109*, A02214, doi:10.1029/2003JA010208.
- Glauert, S. A., and R. B. Horne (2005), Calculation of pitch angle and energy diffusion coefficients with the PADIE code, *J. Geophys. Res.*, *110*, A04206, doi:10.1029/2004JA010851.
- Goldstein, J., B. R. Sandel, W. T. Forrester, M. F. Thomsen, and M. R. Hairston (2005), Global plasmasphere evolution 22–23 April 2001, *J. Geophys. Res.*, *110*, A12218, doi:10.1029/2005JA011282.
- Gonzalez, W. D., B. T. Tsurutani, A. L. C. Gonzalez, E. J. Smith, F. Tang, and S.-I. Akasofu (1989), Solar wind-magnetosphere coupling during intense magnetic storms (1978–1979), *J. Geophys. Res.*, *94*, 8835.
- Goodman, M. L. (1995), A three-dimensional, iterative mapping procedure for the implementation of an ionosphere-magnetosphere anisotropic Ohm's law boundary condition in global magnetohydrodynamic simulations, *Ann. Geophys.*, *13*, 843.
- Gorbachev, O. A., G. V. Khazanov, K. V. Gamayunov, and E. N. Krivovitskiy (1992), A theoretical model for the ring current interaction with the Earth's plasmasphere, *Planet. Space Sci.*, *40*, 859.
- Gringauz, K. I. (1983), Plasmasphere and its interaction with ring current, *Space Sci. Rev.*, *34*, 245.
- Gringauz, K. I. (1985), Structure and properties of the Earth plasmasphere, *Adv. Space Res.*, *5*, 391.
- Gurgiolo, C., B. R. Sandel, J. D. Perez, D. G. Mitchell, C. J. Pollock, and B. A. Larsen (2005), Overlap of the plasmasphere and ring current: Relation to subauroral ionospheric heating, *J. Geophys. Res.*, *110*, A12217, doi:10.1029/2004JA010986.
- Hamilton, D. C., G. Gloeckler, F. M. Ipavich, W. Studemann, B. Wilken, and G. Kremser (1988), Ring current development during the great geomagnetic storm of February 1986, *J. Geophys. Res.*, *93*, 14,343.
- Hardy, D. A., M. S. Gussenhoven, R. Raistrick, and W. J. McNeil (1987), Statistical and functional representation of the pattern of auroral energy flux, number flux, and conductivity, *J. Geophys. Res.*, *92*, 12,275.
- Haselgrove, C. B., and J. Haselgrove (1960), Twisted ray paths in the ionosphere, *Proc. Phys. Soc.*, *75*, 357.
- Haselgrove, J. (1954), Ray theory and a new method for ray tracing, in *Report of Conference on the Physics of the Ionosphere*, 355 pp., Phys. Soc., London.
- Horne, R. B., and R. M. Thorne (1993), On the preferred source location for the convective amplification of ion cyclotron waves, *J. Geophys. Res.*, *98*, 9233.
- Horne, R. B., and R. M. Thorne (1997), Wave heating of  $He^+$  by electromagnetic ion cyclotron waves in the magnetosphere: Heating near  $H^+ - He^+$  bi-ion resonance frequency, *J. Geophys. Res.*, *102*, 11,457.
- Horwitz, J. L., C. R. Baugher, C. R. Chappell, E. G. Shelley, D. T. Young, and R. R. Anderson (1981), ISEE 1 observations of thermal plasma during periods of quieting magnetic activity, *J. Geophys. Res.*, *86*, 9989.

- Iyemori, T., and K. Hayashi (1989), Pc 1 micropulsations observed by Magsat in ionospheric F region, *J. Geophys. Res.*, *94*, 93.
- Jaggi, R. K., and R. A. Wolf (1973), Self-consistent calculation of the motion of a sheet of ions in the magnetosphere, *J. Geophys. Res.*, *78*, 2852.
- Jordanova, V. K., L. M. Kistler, J. U. Kozyra, G. V. Khazanov, and A. F. Nagy (1996), Collisional losses of ring current ions, *J. Geophys. Res.*, *101*, 111.
- Jordanova, V. K., C. J. Farrugia, L. Janoo, J. M. Quinn, R. B. Torbert, K. W. Ogilvie, R. P. Lepping, J. T. Steinberg, D. J. McComas, and R. D. Belian (1998), October 1995 magnetic cloud and accompanying storm activity: Ring current evolution, *J. Geophys. Res.*, *103*, 79.
- Kennel, C. F., and H. E. Petschek (1966), Limit on stably trapped particle fluxes, *J. Geophys. Res.*, *71*, 1.
- Khazanov, G. V., and K. V. Gamayunov (2007), Effect of electromagnetic ion cyclotron wave normal angle distribution on relativistic electron scattering in outer radiation belt, *J. Geophys. Res.*, *112*, A10209, doi:10.1029/2007JA012282.
- Khazanov, G. V., K. V. Gamayunov, and V. K. Jordanova (2003a), Self-consistent model of magnetospheric ring current ions and electromagnetic ion cyclotron waves: The 2–7 May 1998 storm, *J. Geophys. Res.*, *108*(A12), 1419, doi:10.1029/2003JA009856.
- Khazanov, G. V., M. W. Liemohn, T. S. Newman, M.-C. Fok, and R. W. Spiro (2003b), Self-consistent magnetosphere-ionosphere coupling: Theoretical studies, *J. Geophys. Res.*, *108*(A3), 1122, doi:10.1029/2002JA009624.
- Khazanov, G. V., K. V. Gamayunov, D. L. Gallagher, and J. U. Kozyra (2006), Self-consistent model of magnetospheric ring current and propagating electromagnetic ion cyclotron waves: Waves in multi ion magnetosphere, *J. Geophys. Res.*, *111*, A10202, doi:10.1029/2006JA011833.
- Khazanov, G. V., K. V. Gamayunov, D. L. Gallagher, and J. U. Kozyra (2007a), Reply to comment by R. M. Thorne and R. B. Horne on Khazanov et al. [2002] and Khazanov et al. [2006], *J. Geophys. Res.*, *112*, A12215, doi:10.1029/2007JA012463.
- Khazanov, G. V., K. V. Gamayunov, D. L. Gallagher, J. U. Kozyra, and M. W. Liemohn (2007b), Self-consistent model of magnetospheric ring current and propagating electromagnetic ion cyclotron waves. 2. Wave induced ring current precipitation and thermal electron heating, *J. Geophys. Res.*, *112*, A04209, doi:10.1029/2006JA012033.
- Kimura, I. (1966), Effects of ions on whistler-mode ray tracing, *Radio Sci.*, *1*, 269.
- Kozyra, J. U., A. F. Nagy, and D. W. Slater (1997), High-altitude energy source(s) for stable auroral red arcs, *Rev. Geophys.*, *35*, 155.
- LaBelle, J., R. A. Treumann, W. Baumjohann, G. Haerendel, N. Scoppe, G. Paschmann, and H. Lühr (1988), The duskside plasmopause/ring current interface: Convection and plasma wave observations, *J. Geophys. Res.*, *93*, 2573.
- Lepping, R. P., et al. (1995), The Wind magnetic field investigation, *Space Sci. Rev.*, *71*, 207.
- Liemohn, M. W., J. U. Kozyra, V. K. Jordanova, G. V. Khazanov, M. F. Thomsen, and T. E. Cayton (1999), Analysis of early phase ring current recovery mechanisms during geomagnetic storms, *Geophys. Res. Lett.*, *26*, 2845.
- Liemohn, M. W., J. U. Kozyra, C. R. Clauer, and A. J. Ridley (2001), Computational analysis of the near-Earth magnetospheric current system during two-phase decay storms, *J. Geophys. Res.*, *106*, 29,531.
- Liemohn, M. W., A. J. Ridley, D. L. Gallagher, D. M. Ober, and J. U. Kozyra (2004), Dependence of plasmaspheric morphology on the electric field description during the recovery phase of the 17 April 2002 magnetic storm, *J. Geophys. Res.*, *109*, A03209, doi:10.1029/2003JA010304.
- Liemohn, M. W., A. J. Ridley, P. C. Brandt, D. L. Gallagher, J. U. Kozyra, D. M. Ober, D. G. Mitchell, E. C. Roelof, and R. DeMajistre (2005), Parametric analysis of nightside conductance effects on inner magnetospheric dynamics for the 17 April 2002 storm, *J. Geophys. Res.*, *110*, A12S22, doi:10.1029/2005JA011109.
- Lorentzen, K. R., M. P. McCarthy, G. K. Parks, J. E. Foat, R. M. Millan, D. M. Smith, R. P. Lin, and J. P. Treilhou (2000), Precipitation of relativistic electrons by interaction with electromagnetic ion cyclotron waves, *J. Geophys. Res.*, *105*, 5381.
- Lyons, L. R., and R. M. Thorne (1972), Parasitic pitch angle diffusion of radiation belt particles by ion cyclotron waves, *J. Geophys. Res.*, *77*, 5608.
- Mauk, B. H. (1982), Helium resonance and dispersion effects on geostationary Alfvén/ion cyclotron waves, *J. Geophys. Res.*, *87*, 9107.
- Maynard, N. C., and A. J. Chen (1975), Isolated cold plasma regions: Observations and their relation to possible production mechanisms, *J. Geophys. Res.*, *80*, 1009.
- Meredith, N. P., R. M. Thorne, R. B. Horne, D. Summers, B. J. Fraser, and R. R. Anderson (2003), Statistical analysis of relativistic electron energies for cyclotron resonance with EMIC waves observed on CRRES, *J. Geophys. Res.*, *108*(A6), 1250, doi:10.1029/2002JA009700.
- Mishin, E. V., and W. J. Burke (2005), Stormtime coupling of the ring current, plasmasphere and topside ionosphere: Electromagnetic and plasma disturbances, *J. Geophys. Res.*, *110*, A07209, doi:10.1029/2005JA011021.
- Moen, J., and A. Brekke (1993), The solar flux influence on quiet time conductances in the auroral ionosphere, *Geophys. Res. Lett.*, *20*, 971.
- Nishimura, Y., A. Shinbori, T. Ono, M. Iizima, and A. Kumamoto (2007), Evolution of ring current and radiation belt particles under the influence of storm-time electric field, *J. Geophys. Res.*, *112*, A06241, doi:10.1029/2006JA012177.
- Ober, D. M., J. L. Horwitz, and D. L. Gallagher (1997), Formation of density troughs embedded in the outer plasmasphere by subauroral ion drift events, *J. Geophys. Res.*, *102*, 14,595.
- Ober, D. M., J. L. Horwitz, and D. L. Gallagher (1998), Convection of plasmaspheric plasma into the outer magnetosphere and boundary layer region: Initial results, in *Geospace Mass and Energy Flow: Results From the International Solar-Terrestrial Physics Program*, *Geophys. Monogr. Ser.*, vol. 104, edited by J. L. Horwitz, D. L. Gallagher, and W. Peterson, p. 45, AGU, Washington, D. C.
- Ogilvie, K. W., et al. (1995), SWE, A comprehensive plasma instrument for the Wind spacecraft, *Space Sci. Rev.*, *71*, 55.
- Rairden, R. L., L. A. Frank, and J. D. Craven (1986), Geocoronal imaging with Dynamics Explorer, *J. Geophys. Res.*, *91*, 13,613.
- Rasmussen, C. E., and R. W. Schunk (1987), Ionospheric convection driven by NBZ currents, *J. Geophys. Res.*, *92*, 4491.
- Rasmussen, C. E., S. M. Guiter, and S. G. Thomas (1993), Two-dimensional model of the plasmasphere: Refilling time constants, *Planet. Space Sci.*, *41*, 35.
- Richmond, A. D., and Y. Kamide (1988), Mapping electrodynamic features of the high-latitude ionosphere from localized observations: Technique, *J. Geophys. Res.*, *93*, 5741.
- Ridley, A. J., and M. W. Liemohn (2002), A model-derived storm time asymmetric ring current driven electric field description, *J. Geophys. Res.*, *107*(A8), 1151, doi:10.1029/2001JA000051.
- Ridley, A. J., G. Lu, C. R. Clauer, and V. O. Papitashvili (1998), A statistical study of the ionospheric convection response to changing interplanetary magnetic field conditions using the assimilative mapping of ionospheric electrodynamic technique, *J. Geophys. Res.*, *103*(A3), 4023.
- Ridley, A. J., D. L. DeZeeuw, T. I. Gombosi, and K. G. Powell (2001), Using steady state MHD results to predict the global state of the magnetosphere-ionosphere system, *J. Geophys. Res.*, *106*, 30,067.
- Ridley, A. J., T. I. Gombosi, and D. L. DeZeeuw (2004), Ionospheric control of the magnetosphere: Conductance, *Ann. Geophys.*, *22*, 567.
- Sheldon, R. B., and D. C. Hamilton (1993), Ion transport and loss in the Earth's quiet ring current: 1. Data and standard model, *J. Geophys. Res.*, *98*, 13,491.
- Shinbori, A., T. Ono, M. Iizima, and A. Kumamoto (2004), SC related electric and magnetic field phenomena observed by the Akebono satellite inside the plasmasphere, *Earth Planets Space*, *56*, 269.
- Southwood, D. J., and R. A. Wolf (1978), An assessment of the role of precipitation in magnetospheric convection, *J. Geophys. Res.*, *83*, 5227.
- Spasojević, M., J. Goldstein, D. L. Carpenter, U. S. Inan, B. R. Sandel, M. B. Moldwin, and B. W. Reinisch (2003), Global response of the plasmasphere to a geomagnetic disturbance, *J. Geophys. Res.*, *108*(A9), 1340, doi:10.1029/2003JA009987.
- Stern, D. P. (1975), The motion of a proton in the equatorial magnetosphere, *J. Geophys. Res.*, *80*, 595.
- Summers, D., and R. M. Thorne (2003), Relativistic electron pitch angle scattering by electromagnetic ion cyclotron waves during geomagnetic storms, *J. Geophys. Res.*, *108*(A4), 1143, doi:10.1029/2002JA009489.
- Thorne, R. M., and R. B. Horne (1992), The contribution of ion-cyclotron waves to electron heating and SAR-arcs excitation near the storm-time plasmopause, *Geophys. Res. Lett.*, *19*, 417.
- Thorne, R., and R. Horne (1994), Energy transfer between energetic ring current  $H^+$  and  $O^+$  by electromagnetic ion cyclotron waves, *J. Geophys. Res.*, *99*, 17,275.
- Thorne, R., and R. Horne (1997), Modulation of electromagnetic ion cyclotron instability due to interaction with ring current  $O^+$  during the geomagnetic storms, *J. Geophys. Res.*, *102*, 14,155.
- Thorne, R. M., and C. F. Kennel (1971), Relativistic electron precipitation during magnetic storm main phase, *J. Geophys. Res.*, *76*, 4446.
- Tsyganenko, N. A., H. J. Singer, and J. C. Kasper (2003), Storm-time distortion of the inner magnetosphere: How severe can it be?, *J. Geophys. Res.*, *108*(A5), 1209, doi:10.1029/2002JA009808.
- Vasyliunas, V. M. (1970), Mathematical models of magnetospheric convection and its coupling to the ionosphere, in *Particles and Fields in the Magnetosphere*, edited by B. McCormac, p. 60, D. Reidel, Norwell, Mass.



- Vasyliunas, V. M. (1972), The interrelationship of magnetospheric processes, in *Earth's Magnetospheric Processes*, edited by B. McCormac, p. 29, D. Reidel, Hingham, Mass.
- Volland, H. (1973), A semiempirical model of large-scale magnetospheric electric fields, *J. Geophys. Res.*, *78*, 171.
- Weimer, D. R. (1996), A flexible, IMF dependent model of high-latitude electric potentials having "space weather" applications, *Geophys. Res. Lett.*, *23*, 2549.
- Weimer, D. R. (2001), An improved model of ionospheric electric potentials including substorm perturbations and application to the Geospace Environment Modeling November 24, 1996, event, *J. Geophys. Res.*, *106*, 407.
- Wolf, R. A. (1970), Effects of ionospheric conductivity on convective flow of plasma in the magnetosphere, *J. Geophys. Res.*, *75*, 4677.
- Wygant, J., D. Rowland, H. J. Singer, M. Temerin, F. Mozer, and M. K. Hudson (1998), Experimental evidence on the role of the large spatial scale electric field in creating the ring current, *J. Geophys. Res.*, *103*, 29,527.
- Young, D. T., T. J. Geiss, H. Balsiger, P. Eberhardt, A. Ghiedmetti, and H. Rosenbauer (1977), Discovery of  $He^{2+}$  and  $O^{2+}$  ions of terrestrial origin in the outer magnetosphere, *Geophys. Res. Lett.*, *4*, 561.
- Young, D. T., S. Perraut, A. Roux, C. de Villedary, R. Gendrin, A. Korth, G. Kremser, and D. Jones (1981), Wave-particle interactions near  $\Omega_{He^+}$  observed on GEOS 1 and 2, 1, Propagations of ion cyclotron waves in  $He^+$ -rich plasma, *J. Geophys. Res.*, *86*, 6755.
- Young, D. T., H. Balsiger, and J. Geiss (1982), Correlations of magnetospheric ion composition with geomagnetic and solar activity, *J. Geophys. Res.*, *87*, 9077.

---

M.-C. Fok and G. V. Khazanov, NASA Goddard Space Flight Center, Code 673, Greenbelt, MD 20771, USA. (mei-ching.h.fok@nasa.gov; george.v.khazanov@nasa.gov)

K. V. Gamayunov, USRA, NASA Marshall Space Flight Center, 320 Sparkman Drive, Huntsville, AL 35805, USA. (konstantin.gamayunov-1@nasa.gov)

M. W. Liemohn and A. J. Ridley, Atmospheric, Oceanic, and Space Sciences Department, University of Michigan, 2455 Hayward Street, Ann Arbor, MI 49109, USA. (liemohn@umich.edu; ridley@umich.edu)